

# Optical appearance of ices in planet forming discs

Aditya Mahadeva Arabhavi

Technische Universiteit Delft



# Optical appearance of ices in planet forming discs

by

Aditya Mahadeva Arabhavi

to obtain the degree of Master of Science  
at the Delft University of Technology,  
to be defended publicly on Wednesday July 29<sup>th</sup>, 2020 at 10:00 AM.

Student number: 4778057  
Project duration: January 09, 2020 – July 29, 2020  
Thesis committee: Dr. B. R. Brandl, Committee chair  
Dr. S. M. Cazaux, Supervisor (Delft)  
Dr. P. Woitke, Supervisor (St Andrews)  
Dr. B. V. S. Jyoti, Examiner

An electronic version of this thesis will be available at TU Delft Repository from 01/07/2021

Front cover image credits: NASA/JPL-Caltech/R. Hurt (SSC/Caltech)  
About the Object: Artist's impression of the protoplanetary disc NGC 1333-IRAS 4B  
Back cover image credits: NASA/JPL-Caltech/Harvard-Smithsonian CfA  
About the Object: Location of IRAS 4B in the stellar nursery NGC 1333 by Spitzer Space Telescope



# Preface

This work concludes the two years of learning at Delft and St. Andrews, which have been wonderful. I would like to thank all the people who have, directly or indirectly, been a part of this journey.

Firstly, I thank Stephanie for guiding me from the first day. You were the first teacher I talked to at Delft. From attending your lectures, organising Asteroid day, going overtime discussing science during literature study, to supervising my thesis, it has always been a positive and enjoyable experience. I also like to thank you for providing several opportunities to interact and work with experts of different fields. Of course due to which I was able to spend almost a year at St. Andrews. With so many common interests in research and outside research as well, I could not have asked for a better supervisor.

Thank you Peter for providing this great opportunity to work with you at St. Andrews, especially, for taking time to answer every question I had during the internship and thesis. Thank you for making my first astrophysics research interesting, fun and a significant contribution to the field. Under your guidance, I got the opportunity to be a developer in ProDiMo team, to be a part of weekly group meetings and attend journal clubs. Thank you for making this thesis possible with your encouragement, critical feedback, time and support. Again, I could not have asked for a better supervisor.

I would like to thank Jeffrey, Sushen, Shubham and Jordi for being great friends, with whom I shared most of my memorable time at Delft. Thank you for all the laughter, positivity, guidance and bearing through the endless hours of assignments and exams. I would also like to thank Gourav for helping me familiarise things in St. Andrews. I am grateful to all the space flight faculty at TU Delft for designing and delivering this wonderful MSc program. Of course, special thanks to Christiane, Dominic, Oliver, Patrick, Paula, Juan, and rest of the research group members and astro suite for making this project interesting. I also thank the School of Physics and Astronomy, Center for exoplanet science at St Andrews for the opportunity to work with them. I extend my thanks to ProDiMo team members, specially Christian, Inga, Wing-Fai for their inputs which helped a great deal in the research.

Finally, I thank my parents and my brother for always being there for me and always making me feel at home. Thank you for everything.

*Aditya Mahadeva Arabhavi  
Delft, July 2020*



# Abstract

This thesis aims to improve our understanding of the role of ices in planet forming discs, known as protoplanetary discs. Computer models of such discs have been used extensively by the community to understand and predict the observational data. It has always been a challenge to observe ices in the discs and their optical appearance is largely omitted in the disc models. This is due to the complexity and high computational power requirement for computing the opacities while the chemical composition and abundance change at every point in the disc. This work is focused on providing a computationally efficient way of estimating the optical properties of ices in the state-of-the-art Protoplanetary Disk Model (ProDiMo).

Although observations of ices are rare, some observations particularly for the  $3\ \mu\text{m}$  water ice feature are available. These have been studied by means of different radiative transfer disc models, however, the effect of the position-dependent ice opacities on the physico-chemical disc structure has not been considered. In this work, it is found that the optical properties of dust depend on the ice composition, the ice abundances and how the ice accumulates on the refractory dust grains. It is shown that using a pre-calculated opacity grid and performing interpolation between these grid points provides an accurate and computationally efficient estimation of position dependent ice opacities in protoplanetary discs.

Further, it is found that the inclusion of chemically consistent ice opacities calculation in the disc model does not have a significant effect on the physico-chemical structure of the disc. However, the appearance of the disc changes significantly. Dark bands appear in disc images at wavelengths corresponding to ice absorption features. These features are stronger when the thickness of the ice layer on the refractory dust grains is assumed to be constant but weaker when the ice/refractory volume ratio is assumed to be constant. The predicted disc spectra are analysed considering the spatial resolution offered by spectrographic modes of Near-Infrared Spectrograph (NIRSpec) onboard James Webb Space Telescope (JWST), expected to launch in 2021. This shows that the ice features can be observed, particularly when the disc is seen against a distant background source (silhouette discs). Thus, silhouette discs are promising observational targets to study ices in discs.



# Contents

<b>Nomenclature</b> .....	<b>ix</b>
<b>1 Introduction</b> .....	<b>1</b>
1.1 Research Questions .....	2
1.2 Report Outline .....	2
<b>2 Journal Article</b> .....	<b>3</b>
<b>3 Conclusions and recommendations</b> .....	<b>19</b>
3.1 Conclusions .....	19
3.2 Recommendations .....	21
<b>A Position-dependent opacity implementation in ProDiMo</b> .....	<b>23</b>
A.1 ProDiMo flowchart .....	23
A.2 Ice thickness calculation .....	25
A.3 Opacity grid .....	27
<b>B Interpreting the ProDiMo output</b> .....	<b>29</b>
<b>C Verification and Validation</b> .....	<b>31</b>
<b>Bibliography</b> .....	<b>33</b>



# Nomenclature

## Symbols

M	Mass
T	Temperature
V	Volume
r	Radial co-ordinate in cylindrical co-ordinate system
z	Vertical co-ordinate in cylindrical co-ordinate system
$\kappa$	Opacity
$\lambda$	Wavelength
$a$	Bare grain size
$\bar{a}$	Ice covered grain size
Q	Mie efficiency
x	Grain size parameter
f	Normalized grain size distribution
n	Ice powerlaw, coagulation parameter
t	Ice thickness parameter
$n_i$	Number density of species $i$
$\Delta a$	Thickness of ice
$\mu$	Molecular mass
$\rho$	Mass density
m	Complex refractive index
$\theta, \phi$	Logarithmic interpolation weights
$\eta$	Material volume fraction
$A_v$	Visual extinction
F	Flux
$\nu$	Frequency
I	Intensity
J	Mean Intensity
B	Planck Intensity
$\epsilon$	Number of particles per hydrogen nuclei

## Abbreviations and acronyms

ProDiMo	Protoplanetary Disk Model
ALMA	Atacama Large Millimeter/submillimeter Array
JWST	James Webb Space Telescope
SPICA	Space Infrared Telescope for Cosmology and Astrophysics
HST	Hubble Space Telescope
Herschel	Herschel Space Observatory
ISO	Infrared Space Observatory
SED	Spectral Energy Distribution
UV	Ultraviolet
IR	Infrared

NIRSpec      Near InfraRed Spectrograph  
YSO            Young Stellar Object

### Subscripts

r                Radius from the star  
z                Distance above the midplane of the disc  
min             Minimum  
max             Maximum  
pow             Powerlaw  
 $\lambda$             Wavelength  
 $\nu$               Frequency  
I                Ice  
BG              Bare grains  
IG              Icy grains  
d                Dust  
g                Gas  
H<sub>2</sub>O, NH<sub>3</sub>, CO    Ice Species  
CO<sub>2</sub>, CH<sub>4</sub>, CH<sub>3</sub>OH  
H, N, O, C      Elements: hydrogen, nitrogen, oxygen, carbon  
J                Jupiter

# Chapter 1

## Introduction

The first detection of an exoplanet around a main sequence star was made in 1995 (Mayor and Queloz, 1995) and since then there have been 4282 planets catalogued in the Exoplanet-Database (2020) maintained by Paris Observatory. The catalogued planets vary widely in their properties such as mass, orbital eccentricity, semi-major axis, radius of the planet, composition, etc. For example, the mass of exo-planets vary from about  $10^{-3} M_J$  to about  $10^2 M_J$ , where  $M_J$  is the mass of Jupiter. To understand how such diverse set of planets form, it is necessary to study the protoplanetary discs, which are discs around stars where planets are born. These discs are studied by gathering observational data, by numerical modeling and by comparing the model predictions with observations. The observations are performed by various telescopes such as the Atacama Large Millimetre Array (ALMA), the Spitzer Space Telescope (Spitzer), the Infrared Space Observatory (ISO), the Hubble Space Telescope (HST) and, in the future, by various instruments on board the James Webb Space Telescope (JWST) and the Space Infrared Telescope for Cosmology and Astrophysics (SPICA).

Protoplanetary discs can be defined as dense rotating discs of gas and dust around young stars formed after the collapse of a molecular cloud. The mass of the disc is small compared to the star, typically ranging from  $10^{-3}$  to  $10^{-1}$  times the mass of the star (Andrews and Williams, 2005, 2007, Mann and Williams, 2010). However, the angular momentum largely resides in the disc. The discs can be modeled with a Gaussian vertical gas density structure with a radius dependent scale height (Woitke et al., 2016). The distribution of dust in the disc is an equilibrium between upward turbulent mixing and downward gravitational settling (Dubrulle et al., 1995). The temperature profile is largely determined by the amount of stellar radiation intercepted by the disc. The amount of intercepted radiation depends on the disc flaring structure, which is defined by the radial dependence of the vertical gas density scale height. The disc can be broadly divided into two regions: (1) the upper or surface layers, (2) the interior of the disc (Chiang and Goldreich, 1997, Chiang et al., 2001). The scattering properties of dust in the surface layers largely governs the disc temperature in the interior region (Chiang and Goldreich, 1997). The chemical composition of the disc is determined by chemical reactions in the gas phase and on the surface of the dust. The opacity, the scattering and absorption cross sections, of dust in the disc and the radiation intercepted by the disc determine the radiation field within the disc. In shielded regions where the temperature allows for ice formation, the gas phase can accrete on the dust surface (Tielens, 2005). The dynamic processes like viscous evolution, accretion of disc mass onto the star and disc winds determine the evolution of the disc (Armitage, 2010, Williams and Cieza, 2011).

In the disc, dust plays an important role by providing surface for grain surface chemistry for example: Langmuir-Hinshelwood and Eley-Rideal mechanisms, providing surface for ices to accrete, absorbing and scattering radiation, coagulating and acting as seeds for planet formation (Natta et al., 2006, Tielens, 2005). In cold and shielded environments, molecules freeze out on the surfaces of refractory grains to form ices. This not only changes the chemical composition of the dust and gas phase significantly, but also changes the size distribution of grains. For example, for a point in a typical T Tauri disc at a radius of 5 au from the star and close to the midplane (0.12 au above the midplane) the volume of ice is calculated to be  $1.224 \times 10^{-26} \text{ cm}^3/\text{H-nuclei}$ , compared to bare grain volume of  $1.700 \times 10^{-26} \text{ cm}^3/\text{H-nuclei}$ . Similarly, the dust to gas mass ratio changes from 0.015 to 0.0198 upon ice condensation<sup>1</sup>. The optical properties of the dust is determined by the

---

<sup>1</sup>These values are based on a model with bare grain opacities. The ice volume is calculated from the six ice species considered in the thesis. The model is explained in detail in Chapter 2

size distribution and chemical composition (Krugel, 2002). As these properties affect the radiation field in the disc, they can produce observable features when observed with telescopes. Thus, it is important to study the role of ices and dust in protoplanetary discs.

Several disc models are available and can be generally classified as hydrodynamic and thermo-chemical models. The former is used to study the evolution of the disc in time and the latter to study the hydrostatic or the time independent disc structure. The thermo-chemical disc models consistently solve the continuum radiative transfer, dust temperature (Walsh et al., 2014, Woitke et al., 2016). Then the gas phase and ice chemistry is computed, heating/cooling balance is solved to find the gas temperature structure. Based on the consistent solution, other useful data such as spectral energy distribution and images are calculated. In these models, opacities are typically defined based on a refractory grain size distribution, i.e. dust without ices, and hence do not account for the changes in opacity due to ice accretion. To account for the opacities arising from ice accumulation on dust grains, computing ice opacities for each point in the disc is required. However, this is computationally expensive and hence a computationally efficient method of computing ice opacities is required. The goal of this thesis is to improve the disc models by including the effects of ices in cold and shielded environments on the opacity and study the effect of icy dust opacity on the disc structure and appearance. ProDiMo or “Protoplanetary Disc Model” (Woitke et al., 2016) is a thermo-chemical disc model that solves for chemistry, detailed gas heating and cooling balance, and continuum and line radiative transfer in axisymmetric discs. The model uses a 2D physico-chemical grid and assumes axisymmetric disc. The radiative transfer in the disc is solved in 3D. In this thesis, position-dependent ice opacities are implemented in ProDiMo and the role of ice opacities in the disc structure is studied. Then, disc conditions required for observing ice features in these environments with future space observatory such as JWST is explored.

## 1.1 Research Questions

As discussed in the introduction, this work studies the role of ice opacities in protoplanetary discs. The main research question addressed can be formulated as follows:

*What is the role of position-dependent ice opacities in protoplanetary discs and their spectral appearance?*

This can be further broken down into smaller questions as given below.

1. How to implement position-dependent ice opacities in thermo-chemical disc models?
  - (a) What is the position-dependent amount and chemical composition of the ice in protoplanetary discs?
  - (b) How does the thickness of the ice layers depend on grain size distribution?
  - (c) What are the effects of ice formation on continuum opacity?
  - (d) How to calculate the opacities of the icy grains in a computationally efficient way?
2. What are the effects of the opacities of ice-coated grains in protoplanetary discs?
  - (a) What is the effect of position-dependent ice opacities on the physical and chemical structure of the disc?
  - (b) How do the position-dependent ice opacities change the optical appearance of protoplanetary discs from optical to millimeter wavelengths?
  - (c) What are the predictions of observational ice-features for future space-borne telescopes such as JWST and SPICA?

## 1.2 Report Outline

The main research of this thesis is presented as a paper in Chapter 2. The conclusions of this work and recommendations for future work are discussed in Chapter 3. Additional information not included in the journal paper is given in appendices part of the report. Appendix A discusses the technical implementation of position-dependent ice opacities in ProDiMo, including the code structure of ProDiMo, ice thickness calculation, the opacity grid introduced in Chapter 2. The details about using the output from ProDiMo is presented in Appendix B. Verification and validation of the implemented code is discussed in Appendix C.

## **Chapter 2**

# **Journal Article**

The research work has been written in a journal paper format to be submitted to Monthly Notices of Royal Astronomical Society (MNRAS). The manuscript is provided in this chapter using the required template.

# Position-dependent ice opacities in models for protoplanetary discs

Aditya M. Arabhavi,<sup>1,2,4\*</sup> Peter Woitke,<sup>1,4</sup> Stéphanie M. Cazaux<sup>2,3</sup>

<sup>1</sup> School of Physics & Astronomy, University of St. Andrews, North Haugh, St. Andrews KY16 9SS, UK

<sup>2</sup> Faculty of Aerospace Engineering, Delft University of Technology, Delft, The Netherlands

<sup>3</sup> Leiden Observatory, Leiden University, P.O. Box 9513, NL 2300 RA Leiden, The Netherlands

<sup>4</sup> Centre for Exoplanet Science, University of St Andrews, North Haugh, St Andrews, KY16 9SS, UK

## ABSTRACT

Gas phases are known to condense on dust grain surfaces in cold and shielded environments, to form ices such as H<sub>2</sub>O, CO, CO<sub>2</sub>, CH<sub>4</sub>, CH<sub>3</sub>OH and NH<sub>3</sub>. Protoplanetary discs are one such environment where different ice species are distributed with varying abundances, depending on dust temperature and local UV irradiation. We present a new computationally efficient method to compute ice and bare-grain opacities in protoplanetary disc models, using the ice abundances that result from our chemical networks. We discuss the impact of the ice opacities on the physico-chemical state and the optical appearance of the disc. Locally, the opacity can change a lot due to ice formation, especially at UV and optical wavelengths, because ice formation has a distinct effect on the size distribution of small grains. However, since the opacity only changes in the optically thick regions of the disc, the physical disc structure does not change significantly. Our disc models with position-dependent ice opacities provide new insights into the observability of mid-IR ice features, and we discuss favourable configurations and observational setups to observe these features. The spectral energy distributions (SEDs) computed with our new disc models generally do not show significant ice emission or absorption features. However, images of edge-on discs, especially when they are seen against a bright background (silhouette discs), show ice absorption features in certain parts of the image, in particular the dark lane.

**Key words:** protoplanetary discs – opacity – methods: numerical

## 1 INTRODUCTION

Protoplanetary discs are made up of gas and dust with different spatial distribution and temperature structures. The midplane is generally colder and denser for both dust and gas components. In those cold regions, which are well shielded from both stellar and interstellar UV radiation fields, gas phase species can accrete onto dust grain surfaces to form ices. The local thermo-chemical conditions in these regions determine the volume and chemical composition of the forming ice. This ice accretion affects the grain size and composition which are important for opacity calculations (Allamandola et al. 1999; Boogert & Ehrenfreund 2004; Öberg 2009).

Observational data of dust in the diffuse interstellar medium and molecular clouds show the presence of ice covering the dust grains (Kwok et al. 1994; Mathis & Whiffen 1989; Boogert et al. 2008; Goto et al. 2018). For protoplanetary discs, the resolution, spectral range and sensitivity requirements limit the observational capabilities. Though the exact cause of the features are sometimes debatable, absorption features at 3  $\mu\text{m}$  (Honda et al. 2016, 2008; Terada &

Tokunaga 2017; Terada et al. 2007), generally associated to H<sub>2</sub>O ice and emission features at 47  $\mu\text{m}$  and 63  $\mu\text{m}$  (McClure et al. 2015, 2012; Min et al. 2016), generally associated to amorphous and crystalline H<sub>2</sub>O ice respectively, have been observed in discs. Thus, disc modeling becomes important for understanding the properties of icy dust in discs as well as to ascertain the possibility of observing these ices. In disc models, such as in D’Alessio et al. (2006); Semenov & Wiebe (2011); Walsh et al. (2014); Nomura & Millar (2005); Bruderer (2013); Woitke et al. (2016), a grain size distribution is considered with a minimum and maximum grain size, and with a power law with index  $a_{\text{pow}}$  that is fitted to observations, or set to 3.5 power law (MRN-distribution, Mathis et al. (1977)). These grains are considered to be composed of a silicate and a conducting material. Some models consider the presence of ices by using water ice opacities, as for example in Nomura & Millar (2005), however this opacity is based on a separate distribution of water ice grains other than refractory grains and is throughout the disc independent of local irradiation and temperature. This means that the effect of position and abundance of ice species (particularly abundant are H<sub>2</sub>O, CO, NH<sub>3</sub>, CO<sub>2</sub>, CH<sub>3</sub>OH, CH<sub>4</sub>) on opacity, due to the change in both size and composition of the dust grains, has not been considered.

\* E-mail: ama33@st-andrews.ac.uk

Terada et al. (2007) report water ice absorption feature at  $3\ \mu\text{m}$  in edge-on discs HK Tau B and HV Tau C. Terada et al. (2007) also suggest that assuming ice mixtures can explain the absorption features better, such as with CO, CH<sub>4</sub> and CH<sub>3</sub>CN to explain enhanced absorption for  $\lambda \leq 3.0\ \mu\text{m}$  (Brooke et al. 1999; Dartois et al. 2002), CH<sub>3</sub>OH for  $3.54\ \mu\text{m}$  (Smith et al. 1989). Terada & Tokunaga (2017) report the detection of the  $3\ \mu\text{m}$  feature from edge-on circumstellar discs PDS 144N and PDS 453 around Herbig Ae stars. The feature observed from PDS 144N is localized to a radius of 783 au around it and hence argued that it originates from the protoplanetary disc.

McClure et al. (2012) provide the spectra of GQ Lup which shows excess emission near  $63\ \mu\text{m}$ . The best fit model for this data indicates that an icy grain size 2 orders of magnitude larger than silicate grains is needed, which indicates the enhancement of grain sizes due to ice accumulation. Since the disc is highly unsettled, the grains can be mixed between the upper regions and the midplane of the disc. The model computes opacities for graphite and water ice grains assuming that the grains are segregated spheres and that ice exists everywhere below the condensation temperature.

McClure et al. (2015) analyze the emission features at  $47\ \mu\text{m}$  and  $63\ \mu\text{m}$  using the spectroscopic observations of AA Tau, DO Tau and Haro 6-13. The models compute the opacities with an assumption that the grains are segregated. The features are associated to amorphous and crystalline water ice arising from the upper layers of the outer disc regions ( $r > 30\ \text{au}$ ). Since the outer disc regions are colder and crystalline water is not expected in such cold regions, it is indicative of disc heating events or transport processes.

Honda et al. (2008) report presence of H<sub>2</sub>O ice grains on the surface of outer disc region ( $r > 140\ \text{au}$ ) of face-on disc HD 142527 by observing the  $3\ \mu\text{m}$  water ice feature. However, it is also indicated that though these outer regions allow ice condensation, the UV irradiation should make the presence of ice not feasible. Thus, other dynamical process is required to supply the ice to these UV irradiated regions. Min et al. (2016) present Herschel and ISO spectra of HD 142527 which show prominent  $43\ \mu\text{m}$  and  $63\ \mu\text{m}$  crystalline water ice features. The spectra is studied by modeling the disc building up on Verhoeff et al. (2011), a model for HD 142527 disc, using Woitke et al. (2009) to determine the UV field and Min et al. (2009) to solve the radiative transfer. The dust in the disc is assumed to be composed of a mixture of amorphous pyroxene, silica, water and 8 other refractory materials. The  $47\ \mu\text{m}$  and  $63\ \mu\text{m}$  water ice features are used to probe the abundance of water ice in the outer regions of the disc ( $r > 130\ \text{au}$ ) and its crystallinity. HD 142527 is a passive irradiated disc with wall.

Pontoppidan et al. (2005) present spectroscopy and radiative transfer modelling of YSO CRBR 2422.8-3423. The model considers ice opacities which include H<sub>2</sub>O, CO and CO<sub>2</sub> ice species. Further the ice opacities in the model are based on the local temperature. The opacities are defined with a fixed H<sub>2</sub>O ice abundance (or ice thickness). The composition is assumed to be a fixed H<sub>2</sub>O:CO:CO<sub>2</sub> ratio and the is varied by adding inclusion of a fixed CO:CO<sub>2</sub> mixture, keeping the same mantle size. The location of ices in the disc is studied using a radiative transfer model, RADMC (Dullemond & Dominik 2004), and constraints from the ob-

servations data particularly the  $3\ \mu\text{m}$  H<sub>2</sub>O and  $4.67\ \mu\text{m}$  CO ice features.

This paper presents a computationally efficient method of including position dependent opacities in disc models, to account for local ice abundances, and discusses the implications for observations. In Sect. 2 the description of the disc model, ProDiMo, is provided in which the position dependent ice opacities will be implemented. In Sect. 3, the method of calculating position dependent opacities is explained along with the verification of the calculation. The effect of the position dependent opacity on a typical T Tauri disc is discussed in Sect. 4. Section 5 explores what this implementation implies for observations. The method and results are summarised and concluded in Sect. 6.

Appendix A provides details regarding the properties of a typical disc which is considered in this paper. Appendix B summarises the relations of grain composition, size and opacities. Appendix C lists the optical data of different ices used in the model.

## 2 PRODIMO

ProDiMo or Protoplanetary Disk Model (Woitke et al. 2016) is used in this paper to implement the position-dependent dust and ice opacities. The existing model, as explained in Woitke et al. (2016), uses a fixed grain size distribution with no ices. The model starts by setting up the physical state of the disc such as gas and dust densities including dust settling of the bare grains. The code then calculates the dust opacities and solves the continuum radiative transfer problem, including a determination of the dust temperature structure. Subsequently, the code computes the gas phase and ice chemistry and solves the heating & cooling balance to find the gas temperature structure.

The refractory dust grains are assumed to be composed of 60% amorphous silicate (Dorschner et al. (1995), Mg<sub>0.7</sub>Fe<sub>0.3</sub>SiO<sub>3</sub>) and 15% amorphous carbon (Zubko et al. 1996), with a porosity 25%, as discussed in Woitke et al. (2016). The opacity calculations are done by assuming that the grains are spherical and materials are well mixed.

Based on the resulting amounts of ice species formed, the opacities are then recomputed, and the code continues to iterate between radiative transfer, chemistry with ice formation, and opacity calculation, until convergence is achieved. The position-dependent ice abundance and position-dependent settled bare grain size distribution are used to compute new position-dependent grain (bare + ice) size distribution and the grain composition. The recomputation of opacities uses these position-dependent grain composition and position-dependent grain size distribution.

The opacity calculations are based on Mie theory (Bohren & Huffman 2008). The dust grains (including those coated with ice) are considered to be spherical. Ossenkopf & Henning (1994) shows that opacity changed when ice mantles are present on dust grains for a fixed volume of water ice. In this paper, the dependence of ice thickness on grain size is generalised and made computationally easy to apply to disc models. The porosity of the refractory grains and ice layer is fixed to a certain value independent of ice thickness, i.e.,

the possible enhancement or diminution of porosity upon collision and shattering is neglected.

### 3 OPACITY: ICE COMPOSITION, THICKNESS AND REFRACTORY MATERIALS

Opacity ( $\kappa_\lambda$ ) can be defined as the total absorption and scattering cross section of the dust distribution, as shown in Eq. (1):

$$\kappa_\lambda = \int_{a_{min}}^{a_{max}} \pi a^2 Q(a, \lambda) f(a) da \quad (1)$$

where,  $a$  is the grain size,  $a_{min}$  and  $a_{max}$  are the minimum and maximum grain sizes,  $f(a)$  is the considered size distribution ( $= \frac{dN}{da}$ , i.e., number of grains,  $dN$ , per size bin  $da$ ) and  $Q(a, \lambda)$  is the efficiency which is the ratio of absorption and scattering cross section to the geometric cross section of the grain.

Due to ice accumulating on the bare (refractory) grains, both extinction efficiency  $Q(a, \lambda)$  and grain size distribution  $f(a)$  change. These directly affect the opacity  $\kappa_\lambda$ . The effect of ice on these two factors are discussed in the following subsections.

#### 3.1 Effect of ice on size distribution

The abundance of ice, as shown in Fig. A1, varies throughout the disc. This means that the thickness of ice layer differs at each point in the disc. The thickness of ice coating the grains at any point depends on the local volume of ice available and the total grain surface area available for ice accretion at that point in the disc. A simple relation can be written as shown in Eq. (2).

$$V_{IG} = V_I + V_{BG} \\ n_d \int_{a_{min}}^{a_{max}} \frac{4}{3} \pi (a + \Delta a)^3 f(a) da = V_I + n_d \int_{a_{min}}^{a_{max}} \frac{4}{3} \pi a^3 f(a) da \quad (2)$$

where,  $V$  is volume of material per unit volume of space with subscripts  $IG$  for icy grains,  $I$  for ice and  $BG$  for bare grains,  $a$  is the bare grain size,  $\Delta a$  is the ice layer thickness and  $f(a)$  [ $\text{cm}^{-1}$ ] is the normalised size distribution function of the grains,  $a_{min}$  and  $a_{max}$  are the minimum and maximum sizes of the bare grains,  $n_d$  [ $\text{cm}^{-3}$ ] is the number density of grains. If, in Eq. (2),  $\Delta a$  is constant for all grain sizes, then the ice/refractory volume ratio ( $V_I/V_{BG}$ ) is huge for small grains and tiny for large grains. However, icy grains in the midplane can coagulate or shatter. This leads to a uniform ice/refractory volume ratio for grains of different sizes. The limiting case of many such collisions would be an equilibrated, i.e. constant ice/refractory volume ratio of all grains.

In order to allow for a general approach, which includes both limiting cases, we assume that the resulting grains are still spherical. For an icy grain of certain refractory size  $a$ , if  $V_I$ ,  $V_{BG}$  and  $V_{IG}$  are volumes of ice, refractory material and total volume of the icy grain, respectively, the ratio  $\frac{V_I}{V_{IG}}$  or  $\frac{V_{BG}}{V_{IG}}$  (volume fractions of ice or refractory material in an icy grain respectively) differs for grain sizes and depends on

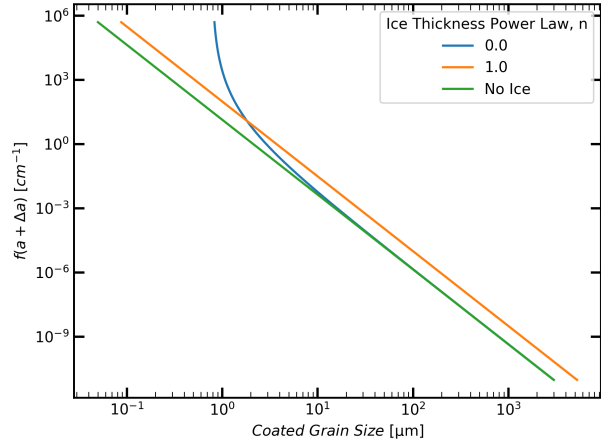


**Figure 1.** Icy grain size distribution for limiting values of ice coating powerlaw. Bare size distribution:  $a_{min} = 0.05 \mu\text{m}$ ,  $a_{max} = 3\text{mm}$ , powerlaw index 3.5,  $V_{BG} = 6.2894 \times 10^{-13} \text{cm}^3$ ,  $V_I = 2.7577 \times 10^{-12} \text{cm}^3$ .

whether icy grains have or have not undergone any coagulation or shattering. In other words, if a grain with refractory size  $a$  is present in an environment where there is no coagulation or shattering, then the ice thickness  $\Delta a$  follows some constant  $t$ . However, if the grain is present in an environment where the grain size distribution has been reached by coagulation, then the ice thickness  $\Delta a$  will be proportional to the size of refractory material,  $t \cdot a$  thus preserving the ice/refractory volume fraction. Similarly, shattering can also be thought of as a ice/refractory volume ratio equalizing process. The following powerlaw approach is used to include both limiting cases

$$\Delta a = t \cdot a^n \quad (3)$$

where,  $t$  and  $n$  are arbitrary coefficients that are indicative of local ice abundance and the local dominance of shattering or collision respectively. The two limiting cases are (1)  $n = 0$ , where the thickness of the ice layer is constant and (2)  $n = 1$ , where the ice/refractory volume fraction is constant and hence the thickness linearly depends on the bare grain size. The values  $0 < n < 1$  relate to cases where the grain size distribution is affected by coagulation or shattering in varying levels. We assume that  $f(a)$  in Eq. (2) is the size distribution of the bare grains.

The effect of the ice covering the dust on the particles (dust + ice) size distribution is shown in Fig. 1. For a constant ice thickness ( $n = 0$ ), the relative increase in size of the smaller grains is several orders of magnitude and the new minimum grain size is determined by the ice layer thickness. The number density of grains of size close to the ice thickness increases significantly. However, the change in size for larger grain sizes is negligible. The overall effect on the grain size distribution is that it does no longer follow a powerlaw. For the other limiting case  $n = 1$ , the small grains have small ice thicknesses and large grains have large ice thicknesses. Both minimum and maximum grain sizes are changed, but this is not as significant as in the case of constant ice thickness. Further, the total grain surface area increases, still dominated by smaller grains, but the size distribution powerlaw is retained.

The total volume of ice at any point in the disc  $V_I$  is ob-

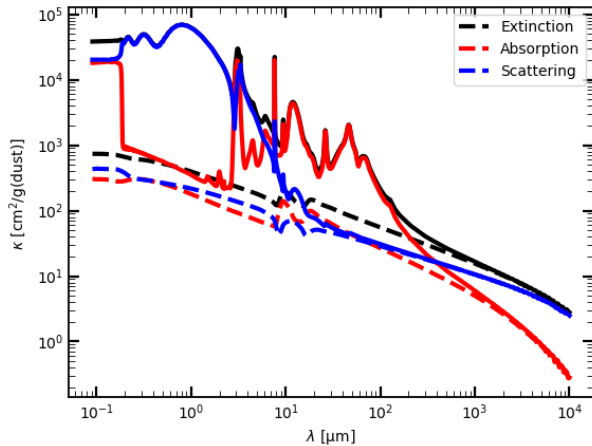


**Figure 2.** Extinction, absorption, scattering opacity of bare grains (dashed) and ice coated grains (solid). A constant thickness of ice layers is assumed for all grains. The composition of grains is  $\text{Mg}_{0.7}\text{Fe}_{0.3}\text{SiO}_3$ , amorphous carbon and porosity in the ratio 0.60:0.15:0.25, and that of ices:  $\text{H}_2\text{O}$ ,  $\text{CH}_4$ ,  $\text{NH}_3$  in the ratio 0.60:0.20:0.20. The volumes of ice and dust being  $1.63 \times 10^{-26} \text{ cm}^3/\text{H}$  and  $4.21 \times 10^{-27} \text{ cm}^3/\text{H}$ . Refractory dust grain size distribution parameters are  $a_{\min} = 0.05 \mu\text{m}$ ,  $a_{\max} = 3 \text{ mm}$ , and powerlaw index 3.5. These opacities have been calculated using effective medium theory.

tained from the chemical output of the disc code. If  $n_i [\text{cm}^{-3}]$  is the number density at a grid point,  $\mu_i [\text{g}]$  is the molecular mass and  $\rho_i [\text{g}/\text{cm}^3]$  is the material mass density of ice species  $i$ , and  $V_i$  is the volume of ice species  $i$ , then the total volume of ice per unit volume of space  $V_I$  at a grid point is given by Eq. (4) for  $N$  ice species.

$$V_i = \frac{n_i \mu_i}{\rho_i} \quad (4)$$

$$V_I = \sum_{i=1}^N V_i$$

Using Eq. (4), Eq. (2) is solved numerically for  $t$  at each grid point in the disc using Newton-Raphson method by approximating the root of the equation  $V_{IG} - V_I - V_{BG} = 0$ , for a given  $n$ .

### 3.2 Effect of ice on extinction, absorption and scattering efficiency

Extinction ( $Q_{\lambda}^{ext}$ ), scattering ( $Q_{\lambda}^{sca}$ ), absorption ( $Q_{\lambda}^{abs}$ ) and radiation pressure ( $Q_{\lambda}^{pr}$ ) efficiencies are related as given in Eq. (5), see Krugel (2002). The extinction and scattering efficiencies are related to the size parameter ( $x = 2\pi a/\lambda$ ) and the complex refractive index  $m(\lambda)$ . These are shown in Eq. (6) (Krugel 2002).

$$Q_{\lambda}^{ext} = Q_{\lambda}^{sca} + Q_{\lambda}^{abs} \quad (5)$$

$$Q_{\lambda}^{pr} = Q_{\lambda}^{ext} - g \cdot Q_{\lambda}^{sca}$$

where,  $g$  is the asymmetry factor, and

$$Q_{\lambda}^{ext} = \frac{2}{x^2} \sum_{n=1}^{\infty} (2n+1) \cdot \text{Re}(a_n + b_n) \quad (6)$$

$$Q_{\lambda}^{sca} = \frac{2}{x^2} \sum_{n=1}^{\infty} (2n+1) \cdot \left[ |a_n|^2 + |b_n|^2 \right]$$

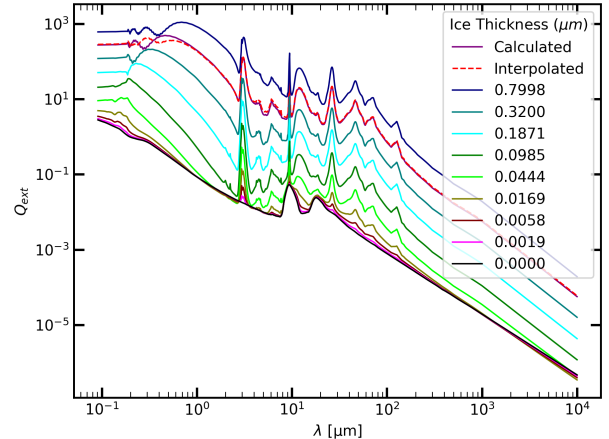


**Figure 3.** Extinction efficiency for a grain size  $0.0559 \mu\text{m}$  (with respect to the bare grain geometrical cross section) with different ice thicknesses composed of  $\text{H}_2\text{O}$ ,  $\text{NH}_3$ ,  $\text{CO}$ ,  $\text{CO}_2$ ,  $\text{CH}_4$ ,  $\text{CH}_3\text{OH}$  in ratio 0.45:0.20:0.10:0.05:0.05:0.15 with 20% of porosity. Also, shows validity of interpolation for constant ice thickness layer of  $0.515 \mu\text{m}$ .

The coefficients  $a_n$  and  $b_n$  are complex functions of  $x$  and complex refractive index  $m(\lambda)$ . These complex functions and the expression for the asymmetry factor can be found in Appendix B.

The default Mie-efficiency calculations in ProDiMo, as explained in Section 2, assume that the same grain material is present everywhere in the disc, i.e. position-independent. In this work, however, at all locations in the disc where the local physical state allows for the presence of ice on grains, the opacity calculations include the increase of size and change of material composition of the grains due to ice formation. Figure A1 shows an example of ice distribution in a typical T Tauri disc. Two factors that should be considered for efficiency calculations are the different ice species and their abundances. The former affects the complex refractive index (and hence the coefficients  $a_n$ ,  $b_n$ ) and latter affects both size and refractive index of the icy grains (and hence the coefficients  $a_n, b_n$  and size parameter  $x$ ). Figure 2 shows the effect of these two factors on extinction, absorption and scattering opacities by assuming a grain size distribution and fixed ice thickness and composition. The figure shows the opacity cross sections per gram of refractory material [ $\text{cm}^2/\text{g}$ ]. Scattering opacity increases both at shorter and longer wavelengths and absorption increases in the mid to far infrared range. Estimating the effects of these two factors, the different ice species and their abundances, on the Mie efficiencies at each grid point are individually explained in the following subsections.

#### 3.2.1 Ice thickness

To estimate the position dependent opacities, a Mie efficiency matrix (Q-matrix) is first generated. Each point in this multi-dimensional matrix is defined by unique ice species, ice thickness, ice power law, grain size and wavelength. A finite number of ice thickness and ice power law values (Eq. 3) are used to populate this matrix. Figure 3 shows how extinction efficiency changes as the thickness of ice layer increases. Since it is computationally expensive

to calculate the efficiencies based on thickness at each grid point using Mie routines, log interpolation (Eq. 7) between points in the pre-calculated Q-matrix is done.

In Eq. (7),  $\theta$  and  $\phi$  are the interpolation weights which define the closeness of the local thickness to the nearest two thickness grid points. However, for interpolation between the grid points of the smallest ice thickness and bare grain opacities, a simple linear interpolation is used. Figure 3 presents the values obtained by such interpolation. It should be noted that in Fig. 3, the efficiency,  $Q_{ext}$ , is the ratio of extinction cross section of ice covered grains to the geometrical cross section of bare grains. Here, bare grain geometrical cross section is considered because it makes the log interpolation of efficiency simple.

$$Q_{a,\lambda}(r,z) = Q_{a,\lambda}(t_1)^\theta \cdot Q_{a,\lambda}(t_2)^\phi$$

$$\theta = \frac{\log(t_2/t_{r,z})}{\log(t_1/t_2)} \quad \phi = \frac{\log(t_1/t_{r,z})}{\log(t_1/t_2)} \quad (7)$$

where,  $r, z$  are the radial distance from the rotation axis and vertical distance from the midplane of a point in disc,  $t_{r,z}$  is the thickness coefficient (see Eq. 3) of ice layer at the location  $(r, z)$  in the disc for which the opacity is being estimated,  $t_1$  and  $t_2$  are the two closest neighbouring points in ice thickness dimension of the pre-calculated Q-matrix, using which the efficiencies  $Q_{a,\lambda}(t_1)$  and  $Q_{a,\lambda}(t_2)$  are obtained from the matrix and  $\theta, \phi$  are the weights for log interpolation. Finally, the values calculated Eq. (7) are scaled by  $(a/\bar{a})^2$  to obtain the actual efficiencies with respect to ice covered grains ( $\bar{a}$  is size of the grain with ice. i.e.,  $\bar{a} = a + \Delta a = a + t_{r,z} \cdot a^{n_{r,z}}$ ). However, the local ice thickness power law ( $n_{r,z}$ ) requires extensive solutions of shattering and coagulation physics and cannot be obtained by disc chemistry. Hence, trivial values ( $n=0,1$ ) are considered in Section 4 independent of position (i.e., same throughout the disc).

### 3.2.2 Ice composition

The protoplanetary discs generally are dominated by  $H_2O$  ice (Öberg et al. 2011). Though the direct observation of ices in discs are scarce, observations of molecular clouds and young stellar objects (YSOs) show the presence of  $H_2O$ , CO,  $CO_2$ ,  $NH_3$ ,  $CH_3OH$ ,  $CH_4$  ice species (Gibb et al. 2004; Boogert et al. 2008; Pontoppidan et al. 2008; Noble et al. 2013; Gibb et al. 2000). These six ice species are considered for opacity calculations in this paper. Our sources for the refractive indices are listed in Appendix C. In this paper, the composition of ice is obtained from the chemical output of the disc code, which is explained in Kamp et al. (2017). This solution does not include grain surface chemistry, however, the ice composition is determined by accretion and desorption processes (including thermal, UV and cosmic ray processes). It is found that the efficiencies based on local ice composition, for a given ice thickness and a given bare grain size distribution, can be approximated by a simple volume fraction weighted summation of efficiencies from the Q-matrix for grains coated with different pure ices. This is shown in Equation 8. This method is computationally efficient because the number of Mie calculations required becomes independent of the spatial grid size of the disc, instead depends on the number of ice species,  $N$ , considered.

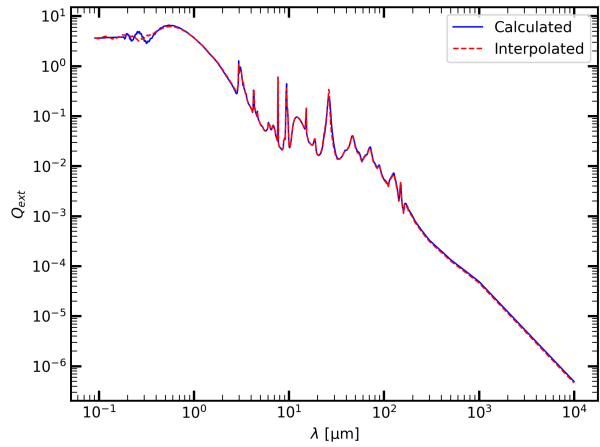


**Figure 4.** Extinction efficiency for a grain size  $0.0559\mu\text{m}$  with  $0.515\mu\text{m}$  ice thickness composed of  $H_2O$ ,  $NH_3$ , CO,  $CO_2$ ,  $CH_4$ ,  $CH_3OH$  in ratio 0.16:0.16:0.16:0.2:0.16:0.16 with 20% of porosity.

$$Q_{a,\lambda}(Bare, Ice_1, Ice_2, \dots, Ice_n) = \sum_{i=1}^N (\eta_i Q_{a,\lambda}(Bare + Ice_i)) \quad (8)$$

where,  $Q_{a,\lambda}$  is the efficiency, the left hand side of the equation is the efficiency of the grains coated with local mixed ice, composed of species 1 to  $N$ ,  $\eta_i$  is their respective ice volume fraction ( $\eta_i = V_i/V_I$ , Eq. 4). It should be noted that in Eq. (8), the  $Q_{a,\lambda}$  on LHS and RHS are based on the same refractory grain composition and size. The validity of this approach is shown in Figure 4, which compares the efficiencies calculated for grain coated with a mixed ice layer (1) by using effective medium theory for ice mixture and (2) by weighted summation as given in Equation 8. The figure shows that the interpolation is in agreement with calculation using effective medium Mie routine.

### 3.3 Effective medium vs core-mantle Mie theory

The composition of the icy grains can be thought of as (1) a mixture of ices and refractory material or (2) a multi-layered structure with refractory material as the core and an ice mantle on top. The opacity calculations for these two cases can be carried out using either Mie theory with effective medium theory or core-mantle Mie theory, respectively. However, the computational effort required for core-mantle solutions is a factor 4 greater than the other.

It can be argued that in the limiting case  $n = 1$ , the coagulated/shattered grains do not retain a core-mantle structure. Further, it is debatable whether icy grains are layered or mixed in disc environments. For example, ices could be organised as layers starting with a layer of polar ices such as  $H_2O$ ,  $NH_3$  and  $CH_3OH$  and on top a layer of non-polar ices such as CO,  $N_2$  and  $O_2$ , creating an onion-like structure (Öberg 2009). Ice covered grains can undergo processing due to thermal processes, ultraviolet photos and cosmic ray particles, called energetically processed ice (Boogert et al. 2015), which can mix the ices in the mantle and as well

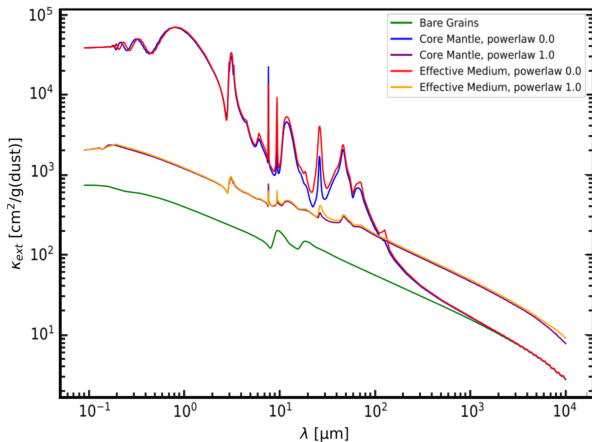


**Figure 5.** Extinction opacity of bare grains and ice covered dust grains calculated using the effective medium theory and Core-Mantle Mie theory for ice powerlaws 0 and 1. The ice composition is  $\text{H}_2\text{O}:\text{NH}_3:\text{CH}_4:\text{Vacuum} = 0.51:0.40:0.04:0.05$ . The volume of ice, bare grain size distribution and composition is same as in Fig. 1

cause segregation. Impinging energetic particles and irradiation with X-rays and UV photons may cause ice desorption (Palumbo et al. 2006; Andersson & Van Dishoeck 2008; Fayolle et al. 2014), mantle explosion (Ivlev et al. 2015) or the formation of new ice species Garrod et al. (2008), possibly followed by molecular ejections which can lead to mixed ices (Dulieu et al. 2013). The mixed ice components can again undergo processing leading to ice restructuring and segregation (Fayolle et al. 2011; Öberg et al. 2009b). Further, thermal and radiative processes can also form larger and more complex molecules (Garrod et al. 2008; Gerakines et al. 1996; Öberg et al. 2009a; Caro et al. 2002). In the present model, neither ice segregation nor grain surface chemistry is considered. Moreover, using Eq. (8) does not take into account the ice features that result from interactions between different ice phases, for example  $\text{CO-H}_2\text{O}$  at  $4.68 \mu\text{m}$ ,  $4.647 \mu\text{m}$  (Tielens et al. 1991; Sandford et al. 1988). Figure 5 shows the ice opacities calculated for the limiting ice powerlaws with effective medium theory and core-mantle Mie theory. The differences between the opacity values calculated by these two approaches are small. Due to these reasons our opacity calculations are based on effective medium theory.

#### 4 IMPACT OF ICE OPACITIES ON THE OPTICAL APPEARANCE OF T TAURI DISCS

In the following, we discuss three protoplanetary disc simulations with identical settings of stellar, disc shape and mass, settling and bare grain parameters for a T Tauri setup, see Table A. The models only differ with respect to the treatment of the ice opacities. The position-dependent icy grain opacity calculations are based on the abundances of ice species as provided by the chemical network at each point in the disc. The iteration between chemistry, opacity calculation and continuum radiative transfer, as described in Sect. 2, is continued until the opacity computations converge to a tolerance of less than 5%.

#### 4.1 Extinction and opacity

The inclusion of the ice opacities significantly changes the extinction properties of the disc in the model, in particular in the midplane where ices are abundant. Panels A-E in Fig. 6 show different properties of the disc in three models: (1) ice opacities for a constant ice thickness,  $n = 0$ , plotted with solid lines, (2) ice opacities for a grain size dependent ice thickness,  $n=1$ , with dotted lines, and (3) no ice opacities (just bare grain opacities) with dashed lines. Panel F of Fig. 6 shows the disc mass averaged opacity of a typical T Tauri disc [in  $\text{cm}^2/\text{g}(\text{refractory material})$ ] with bare grains, constant thickness ice coated grains and constant ice/refractory volume ratio grains. The bare grain model shows two silicate features at  $10 \mu\text{m}$  and  $20 \mu\text{m}$ . The constant ice/refractory volume ratio model shows small features around  $3 \mu\text{m}$  ( $\text{H}_2\text{O}$ ),  $4 \mu\text{m}$  ( $\text{CO}_2$ ),  $30 \mu\text{m}$  ( $\text{NH}_3$ ) and the silicate features. The opacity is larger at shorter wavelengths ( $<10 \mu\text{m}$ ) compared to the bare grain model. The constant ice thickness layer model shows a much more significant increase at short wavelengths, about one order of magnitude in the visible range. Furthermore, the ice features are enhanced significantly, prominently showing  $\text{H}_2\text{O}$ ,  $\text{NH}_3$ ,  $\text{CO}_2$ ,  $\text{CO}$  and  $\text{CH}_4$  features. Hence, the average opacity of the disc strongly depends on the ice power law,  $n$ , in Equation 3. The ice abundances using the position dependent opacities is shown in Fig. A2. The figure shows (in comparison with Fig. A1) that the water ice dominated region is extended from 8 au to 23 au and on the other hand, the  $\text{CO}$  ice region is pushed beyond 100 au.

Panels A and B show the effect of the ice opacities on the radial and vertical optical depths. When ice opacities are included, the vertical extinction increases significantly towards the midplane, but only once the disc has become optically thick. This increase is particularly strong in the  $n=0$  model, where the opacity increase very suddenly, like an opacity wall or barrier. This behaviour is mostly a size effect, because ice formation increases the sizes of the small grains in particular, which are the carrier of the opacity at optical wavelengths. For example, the vertical optical extinction at 30 au in the midplane changes from about 10 to 100 when  $n = 0$  ice opacities are considered. Another example is the radial extension of the disc as measured by the condition that the vertical optical depth across the disc is one at optical wavelengths, which increases from about 120 au for the bare grain model to about 300 au for the  $n=0$  model. The impact of the icy opacities in the  $n = 1$  model is less pronounced. Hence, the extinction profile in the disc strongly depends on the relation between the ice thickness and grain size, i.e. the ice power law index  $n$  in Eq. (3).

#### 4.2 SED and temperature profile

Although the mean opacities in the disc increase quite dramatically when ice coating is included, the main disc properties such as temperature, pressure and chemical abundances, etc., do not change significantly in the models. This is because the ice only builds up in the (radially and vertically) optically thick and shielded regions in the disc. In particular, there is almost no ice in the model at places into which stellar or interstellar UV photons can penetrate, even if the local dust temperatures are low. This is because of the UV

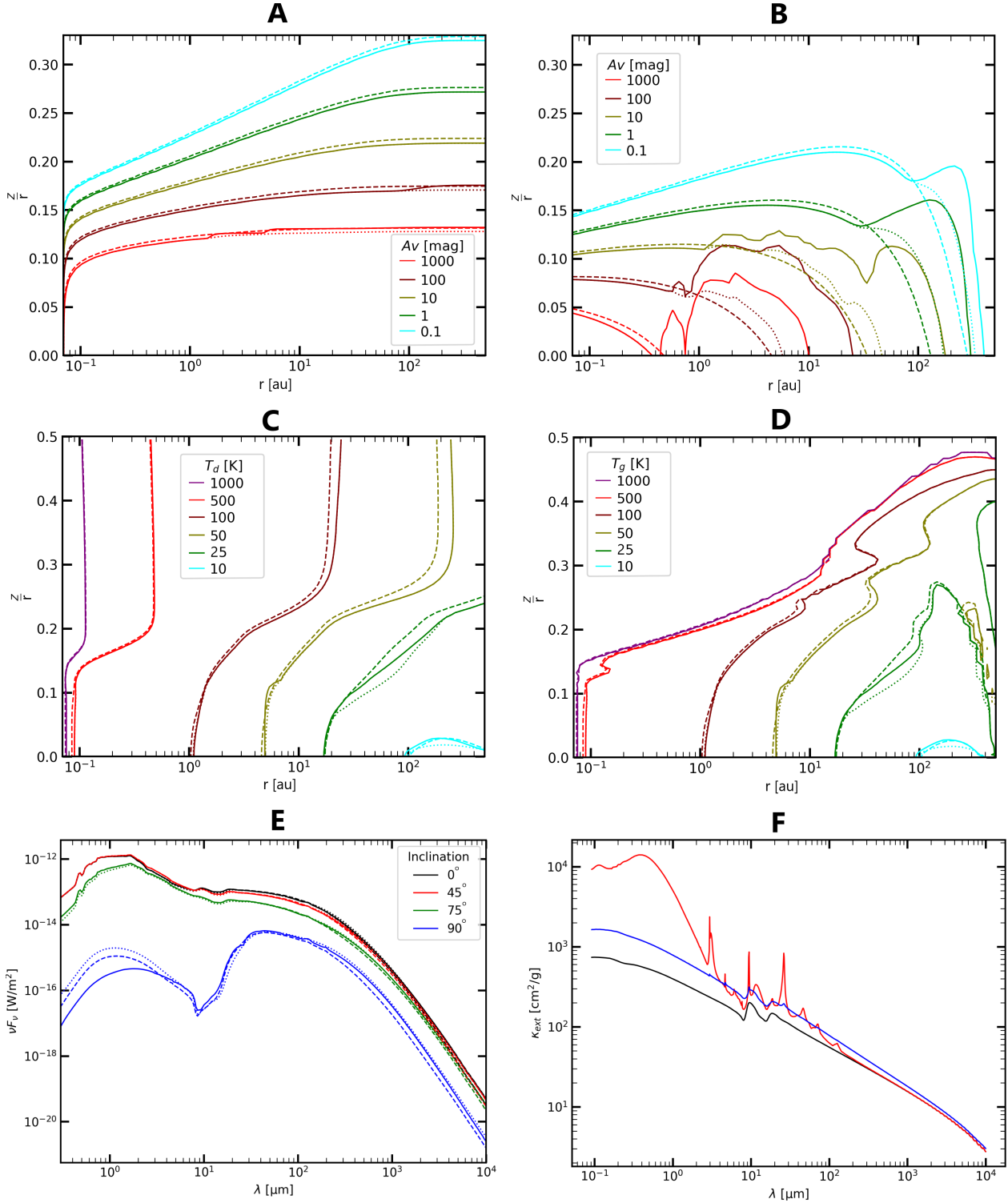


**Figure 6.** From A-E, Visual extinction (vertical), visual extinction (horizontal), dust temperature, gas temperature, spectral energy distribution, with *dashed*: bare grains, *solid*: icy grains with constant thickness of ice layer ( $n=0$ ), *dotted*: icy grains with constant ice/refractory volume ratio ( $n=1$ ). Panel F shows mass average extinction opacity in the disc with *black*: bare grains, *red*:  $n=0$ , *blue*:  $n=1$ . The opacities are relative to the total mass of refractory grains in the disc.

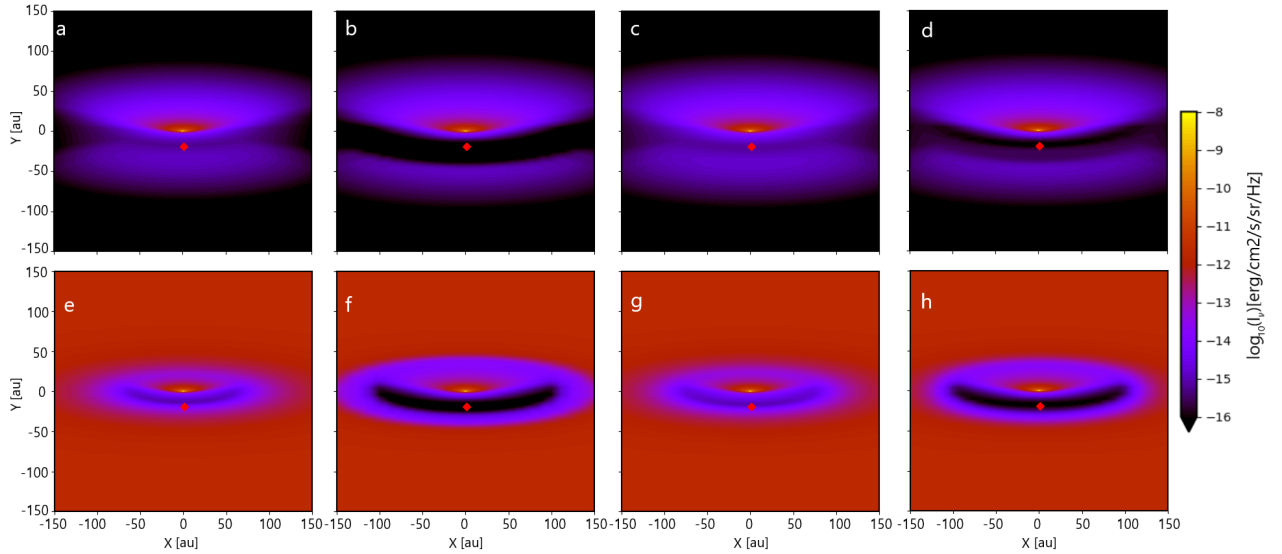


**Figure 7.** Simulated images (intensity maps) at  $26\ \mu\text{m}$  and inclination of  $75^\circ$  from four consistent icy disc models with different opacity treatment, (a) bare grain disc model (model 1), (b) constant ice thickness model  $n = 0$  (model 2), (c) constant ice/refractory volume ratio model  $n = 1$  (model 3), (d)  $n = 1$  in midplane ( $z/x < 0.1$ ) and  $n = 0$  elsewhere (model 4). Bottom row (e-h) of images are the same disc models as in the top row (a-d), but when seen against a bright uniform infrared background (silhouette discs).

photo-desorption process, which removes icy species as they interact with UV photons. The changes of opacity in the optically thick regions have no significant influence on the local mean intensities ( $J_\nu$ ), as  $J_\nu \approx B_\nu(T_d)$  is valid anyway ( $B_\nu$  is the Planck or black-body radiation), and hence there is no significant influence on the radiation that escapes from these regions. Panels C and D of Fig. 6 show the computed dust and gas temperatures in the three disc models. Models that include position-dependent ice opacities (solid and dotted) are cooler than bare grain opacity model (dashed) in terms of both dust and gas. This is because the models with ice opacities scatter incoming radiation more than the model with bare grain opacity. Due to scattering, the amount of radiation absorbed by the dust and thereby increasing the temperature is small compared to bare grain model. Since there is almost no ice in the upper regions of the disc, the temperature differences are small.

The spectral energy distributions (SEDs) of the three models are presented in panel E of Fig. 6 for disc inclinations  $0^\circ$ ,  $45^\circ$ ,  $75^\circ$  and  $90^\circ$ . The surface layer of the disc re-emits or scatters radiation received from the star toward the observer and toward the disc midplane (Natta 1993). The latter largely determines the temperatures in the disc (Chiang & Goldreich 1997; Chiang et al. 2001). Since there is practically no ice in these surface layers, the visual extinction and the albedo in the disc surface remain unaffected, and hence the temperatures in the disc do not change significantly. Thus, we do not see ice emission features in the disc flux spectra. However, at higher inclinations the flux at shorter wavelengths ( $< 3\ \mu\text{m}$ ) for the case  $n = 0$  is about an order of magnitude smaller compared to bare grain model.

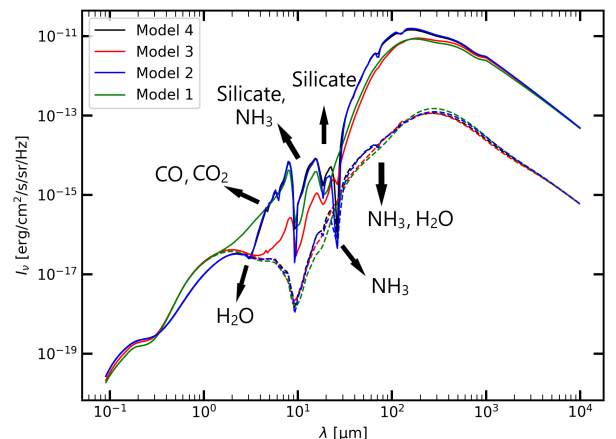


**Figure 8.** Intensity spectra for the point marked by red diamonds in Figure 7. Solid line - silhouette discs, dashed line - discs without background source.

## 5 OBSERVING THE ICE FEATURES

Although the effect of ice opacities on the physical disc structure is small, it is interesting to discuss whether it is possible to observe the ice signatures, which would provide important insights into the nature of the ices in protoplanetary discs.

Figure 7 shows simulated images at  $26\ \mu\text{m}$  (at the centre of a strong  $\text{NH}_3$  ice feature), computed from four disc models. Model 1 is the model with bare grain opacity. Model 2 is the model with ice opacities for case  $n = 0$ . Model 3 is the model with ice opacities for case  $n = 1$ . Model 4 is constructed with different opacity options in two regions: the first region is the midplane ( $z/r < 0.1$ ) with  $n = 1$  ice opacities, and the second region is above the midplane with  $n = 0$  ice opacities. As explained in subsection 3.1, the dominance of coagulation or shattering can significantly change the grain

size distribution. Since the number density of grains in the midplane increases due to dust settling, the dominance of coagulation or shattering can be very different in the midplane compared to outside the midplane. Hence, model 4 assumes a coagulated midplane and an uncoagulated environment outside the midplane. Panels (a)-(d) in Fig. 7 show simulated images from these 4 disc models without a background, and panels (e)-(f) show the images of the same 4 models, but against a bright uniform IR background source. For the discs with background, first, the disc model is calculated without the IR background. Then, for ray tracing to generate the images, the IR background is considered on and the dust temperatures are fixed. The physical idea behind this approach is based on the assumption that the disc sees only a small solid angle of this background radiation and thus it does not affect the radiation field within the disc unlike protoplanetary discs. For these models the IR background field, given by Mathis et al. (1983), is scaled by a factor such that a blackbody in this isotropic background field would have a temperature of 100 K.

Panel B of Fig. 6 shows that the inclusion of ice opacities extends the extinction radially. Thus, a disc with ice opacities appears larger, in particular in absorption, than a bare grain disc. We see that the icy discs appears larger in absorption, in particular when the ice opacities are computed with the constant ice thickness option  $n=0$  (Fig. 7 Panels b and f). The constant ice thickness model shows a distinct band of absorption around the midplane, subsequently called the dark lane. The dark lane is seen with higher contrast when silhouette discs, i.e. discs with a background source, are considered.

Intensity spectra of a single point in the dark lane (shown by red dots in Fig. 7) for different models are shown in Fig. 8. The figure shows the intensity spectra for silhouette discs (solid lines) and discs without background (dashed lines). The spectra of all the four models are similar. However, the spectra of the models with ice opacities shows ice features, and these features are stronger for models 3 and 4. For the discs without background, the features of  $\text{NH}_3$  are seen at  $26 \mu\text{m}$  and  $70 \mu\text{m}$ . These absorption features are more pronounced in silhouette discs, and the spectra (Fig. 8) shows other strong absorption features such as  $\text{H}_2\text{O}$  at  $3 \mu\text{m}$ ,  $\text{CO}_2$  and  $\text{CO}$  at  $4.6 \mu\text{m}$ ,  $\text{NH}_3$  at  $9 \mu\text{m}$ , and silicate features at  $10$  and  $20 \mu\text{m}$ . This is because, for a disc without a background, the midplane is cold and the intensity from the disc at shorter wavelengths is very small. However, the background source for silhouette discs provides sufficient intensity at wavelength where ice absorption features appear. For model 3, i.e., when  $n=1$ , the ice features become weaker compared to models 2 and 4. This can be explained by the effect of ice power law on the opacity as seen in Fig. 5, i.e. the opacity increase is more uniform in wavelength space but the ice features appear significantly less pronounced compared to the case with constant ice thickness. Thus, the ice power-law and background radiation source become important parameters which affect the appearance of the ice features.

Figure 7 (panels d and h) and Fig. 8 show that the zoned model 4 appears rather similar to model 2. Although model 4 assumes a constant ice/refractory volume ratio ( $n=1$ ) in the midplane, the observable properties are very similar to model 2, which assumes a constant ice layer thickness ( $n=$

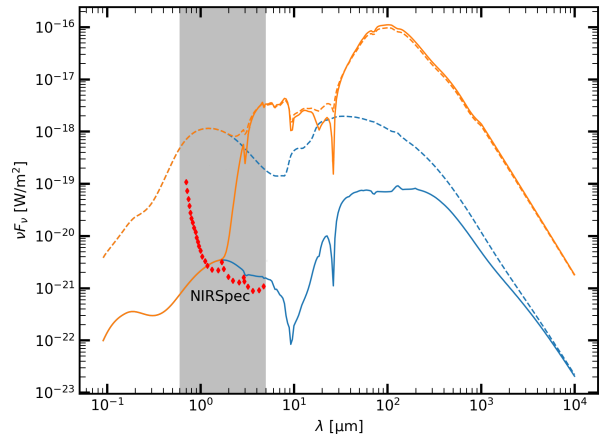


**Figure 9.** Flux of model 2 in a single pixel at a spatial resolution corresponding to the JWST NIRSpect spectroscopy modes (dashed: single slit mode, solid: microshutters mode) for the distance of disc = 140 pc. The shaded region shows the wavelength range covered by NIRSpect. Blue: Normal disc. Orange: Silhouette disc. The red dots indicate the limiting sensitivity of NIRSpect instrument.

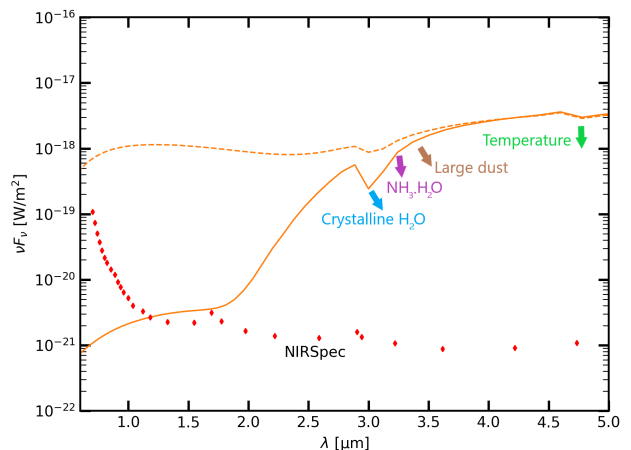


**Figure 10.** Flux spectra corresponding to the resolution and wavelength range of NIRSpect for the silhouette discs in Fig. 9

0) everywhere. This suggests that the ice signal originates mostly from layers above the midplane where model 4 also assumes  $n=0$ . The ice opacity in the core of the midplane has little effect on the observable ice features. Thus, comparing models 2, 3 and 4 tells us that the spectral appearance of ice features is an indicator of the relation between grain size and ice thickness.

Figure 8 shows ice features in the intensity spectra of one point in the simulated disc image when seen under large inclination angles, the selected point is marked in Fig. 7. However, when observing discs, the spatial resolution of the telescope depends on the numbers of pixels used to map the source, the instrument specifications, and the distance of the disc (which is assumed to be 140 pc in this paper similar to the distance of  $\rho$ -Ophiuchus (De Zeeuw et al. 1999), one of the closest star forming regions to the solar system). The single slit spectroscopy mode of NIRSpect

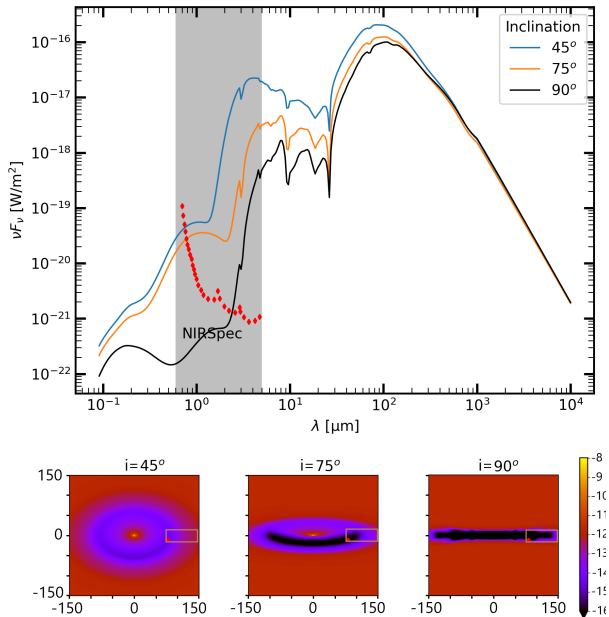


**Figure 11.** Flux of model 2 in a single pixel at a spatial resolution corresponding to the JWST NIRSpec spectroscopy modes for the distance of disc = 140 pc at inclination angles 45°, 75°, 90°. The shaded region shows the wavelength range covered by NIRSpec. The red dots indicate the limiting sensitivity of NIRSpec instrument. Bottom panels show the images (at 26  $\mu\text{m}$ ) of the disc model at different inclinations and the brown boxes show the position of the pixel of which the flux is plotted.

(JWST) has a slit size of  $0.6'' \times 5.5''$  and the microshutter mode has the field of view of  $3.4' \times 3.4'$  which is composed of 250,000  $0.2'' \times 0.5''$  microshutters (at the assumed distance of the source,  $1'' = 140$  au). The spectral data at higher spatial resolution from ProDiMo is then converted into data at spatial resolution (pixelated) of the observation modes of NIRSpec. The spectral data of pixel that contains the red dot from Fig. 7 is then plotted in Fig. 9. The spectral range of NIRSpec is 0.6–5.0  $\mu\text{m}$ , which is highlighted in gray in the Fig. 9. The figure shows the spectra for model 2 with (orange) and without (blue) background source. With a spatial resolution of both single slit (dashed line) and microshutter (solid line) spectroscopy modes, the 3  $\mu\text{m}$  feature can be observed, though the microshutters mode provides better contrast of the feature.

Figure 10 shows the spectra of the silhouette disc from Fig. 9 in the wavelength range of NIRSpec. Terada et al. (2012) observed 3  $\mu\text{m}$  H<sub>2</sub>O feature from d216-0939 and d132-1832, silhouette discs, in Orion Nebula Cluster with Subaru Adaptive Optics system. The position dependent ice opacity model can be used to predict and fit such ice features. The features shown in Fig. 10, i.e., the 3  $\mu\text{m}$  H<sub>2</sub>O and 4.6  $\mu\text{m}$  CO ice features can provide information regarding the ice composition and thermal processing. The 4.6  $\mu\text{m}$  is composed of two bumps related to CO in apolar and polar ice matrix at 4.67  $\mu\text{m}$  and 4.68  $\mu\text{m}$  respectively (Sandford & Allamandola 1988). A smaller feature at 4.64  $\mu\text{m}$  appears at very low temperatures, all these CO features decrease with increase in temperature (Sandford & Allamandola 1988). These fea-

tures change significantly with irradiation and temperature (Palumbo & Strazzulla 1993; Sandford & Allamandola 1988; Boogert et al. 2015). Further, if the H<sub>2</sub>O ice is crystalline, the 3  $\mu\text{m}$  water feature is more peaked or sharp. Having NH<sub>3</sub>·H<sub>2</sub>O hydrates or larger dust grains broadens the shape of the long-wavelength part of the feature (Boogert et al. 2015) as indicated in Fig. 10.

Figure 11 shows the flux spectra of model 2 ( $n = 0$ ) at the spatial resolution of NIRSpec microshutter mode at 45°, 75° and 90° inclinations of the disc. The bottom panels in the figure show the images of the discs at the mentioned inclinations and the pixel for which the spectra is plotted. The ice features are generally enhanced with increasing inclination. The column density of ice observed per pixel or solid angle increases with increasing inclination. Thus, the radiation captures the ice signals strongly enhancing the features at higher inclinations. The 3  $\mu\text{m}$  water ice feature is diminished at inclination of 90° because the intensity itself drops due to high optical depths. Thus, we show here that our model predicts that ices can be observed in silhouette discs with the spatial resolution of microshutter mode of JWST NIRSpec instrument.

## 6 CONCLUSIONS

A computationally efficient way of computing position-dependent ice and bare grain opacities in protoplanetary discs has been implemented in ProDiMo. The main conclusions are

(i) The presented models consistently couple chemistry, ice formation, opacity computations, and radiative transfer in protoplanetary discs.

(ii) Locally, the continuum opacity can change significantly by ice formation. The opacity changes are particularly large at shorter wavelengths, mostly because of the increased size of the small grains, when assuming a constant ice coverage on all grains. Opacity changes are less pronounced, and more uniform in wavelength space, when the grains are assumed to have a constant ice/refractory volume ratio, which is expected if coagulation and shattering are important. In both cases, the primary reason for those opacity changes is the altered size distribution of the icy grains.

(iii) A weighted sum of the opacities of the different pure ices and log interpolation of opacities between pre-calculated points in ice thickness space provides a computationally efficient and sufficiently accurate method to calculate the icy opacities in protoplanetary discs.

(iv) The position-dependent ice opacities do not alter the physical disc structure significantly, because the ice opacities are only present in optically thick region of the disc.

(v) Infrared ice features from the disc prove difficult to detect, they can neither be seen in absorption nor in emission according to our models, when observing the total flux of the disc. Previous detections such as McClure et al. (2012, 2015); Terada & Tokunaga (2017) are likely to be related to envelopes rather than discs or the observed discs have dynamical processes that transport icy grains to regions well above the midplane where radiation can penetrate and ices can be seen. Such a process can be transport of ices to upper regions of the disc by turbulence or or by an out-gassing comet.

(vi) Using our models, the discs appear larger in absorption than discs with bare grains only, and show a more prominent dark lane in resolved images. This dark lane is caused by icy grains situated just above the disc midplane, and the darkness of the lane depends on the assumptions used to calculate the modified dust size distribution.

(vii) Our models predict that the ice absorption features in the near and mid infrared wavelengths can be observed from the dark lanes by spectroscopy with sufficient resolution, example JWST NIRSpec microshutter spectroscopy mode, for a typical disc at 140 pc. These features are greatly enhanced when a background source is present. Hence, silhouette discs are better targets to observe ice features. These features are further enhanced at higher disc inclinations.

## REFERENCES

- Allamandola L. J., Bernstein M. P., Sandford S. A., Walker R. L., 1999, in , *Composition and Origin of Cometary Materials*. Springer, pp 219–232
- Andersson S., Van Dishoeck E., 2008, *Astronomy & Astrophysics*, 491, 907
- Bohren C. F., Huffman D. R., 2008, *Absorption and scattering of light by small particles*. John Wiley & Sons
- Boogert A., Ehrenfreund P., 2004, in *Astrophysics of Dust*. p. 547
- Boogert A. C., et al., 2008, *The Astrophysical Journal*, 678, 985
- Boogert A. A., Gerakines P. A., Whittet D. C., 2015, *Annual Review of Astronomy and Astrophysics*, 53
- Brooke T., Sellgren K., Geballe T., 1999, *The Astrophysical Journal*, 517, 883
- Bruderer S., 2013, *Astronomy & Astrophysics*, 559, A46
- Bruggeman V. D., 1935, *Annalen der Physik*, 416, 636
- Cai W., 2019, *Characterization of composite nanoparticles using an improved light scattering program for coated spheres*
- Caro G. M., et al., 2002, *Nature*, 416, 403
- Chiang E., Goldreich P., 1997, *The Astrophysical Journal*, 490, 368
- Chiang E., Joungh M., Creech-Eakman M., Qi C., Kessler J., Blake G., Van Dishoeck E., 2001, *The Astrophysical Journal*, 547, 1077
- Dartois E., d'Hendecourt L., Thi W., Pontoppidan K., Van Dishoeck E., 2002, *Astronomy & Astrophysics*, 394, 1057
- Dave J., 1968, *Subroutines for computing the parameters of the electromagnetic radiation scattered by a sphere*. IBM Palo Alto Scientific Center
- De Zeeuw P., Hoogerwerf R. v., de Bruijne J. H., Brown A., Blaauw A., 1999, *The Astronomical Journal*, 117, 354
- Dorschner J., Begemann B., Henning T., Jaeger C., Mutschke H., 1995, *Astronomy and Astrophysics*, 300, 503
- Dulieu F., Congiu E., Noble J., Baouche S., Chaabouni H., Moudens A., Minissale M., Cazaux S., 2013, *Scientific Reports*, 3
- Dullemond C., Dominik C., 2004, *Astronomy & Astrophysics*, 417, 159
- D'Alessio P., Calvet N., Hartmann L., Franco-Hernández R., Servín H., 2006, *The Astrophysical Journal*, 638, 314
- Fayolle E. C., Öberg K., Cuppen H. M., Visser R., Linnartz H., 2011, *Astronomy & Astrophysics*, 529, A74
- Fayolle E., Bertin M., Romanzin C., Michaut X., Philippe L., Öberg K. I., Linnartz H., Pillion J.-H., 2014, in *American Astronomical Society Meeting Abstracts #224*. p. 205.04
- Garrod R. T., Weaver S. L. W., Herbst E., 2008, *The Astrophysical Journal*, 682, 283
- Gerakines P., Schutte W., Ehrenfreund P., 1996, *Astronomy and Astrophysics*, 312, 289
- Gibb E., et al., 2000, *The Astrophysical Journal*, 536, 347
- Gibb E., Whittet D., Boogert A., Tielens A., 2004, *The Astrophysical Journal Supplement Series*, 151, 35
- Goto M., Bailey J. D., Hocuk S., Caselli P., Esplugues G. B., Cazaux S., Spaans M., 2018, *Astronomy & Astrophysics*, 610, A9
- Honda M., et al., 2008, *The Astrophysical Journal Letters*, 690, L110
- Honda M., et al., 2016, *The Astrophysical Journal*, 821, 2
- Hudgins D., Sandford S., Allamandola L., Tielens A., 1993, *The Astrophysical Journal Supplement Series*, 86, 713
- Ivlev A., Röcker T., Vasyunin A., Caselli P., 2015, *The Astrophysical Journal*, 805, 59
- Kamp I., Thi W.-F., Woitke P., Rab C., Bouma S., Menard F., 2017, *Astronomy & Astrophysics*, 607, A41
- Krugel E., 2002, *The physics of interstellar dust*. CRC Press
- Kwok S., Hrivnak R., Geballe T., Langill P., 1994, *Astronomical Infrared Spectroscopy: Future Observational Directions*, ASP Conf
- Martonchik J. V., Orton G. S., Appleby J. F., 1984, *Applied optics*, 23, 541
- Mathis J. S., Whiffen G., 1989, *The Astrophysical Journal*, 341, 808
- Mathis J. S., Rumpl W., Nordsieck K. H., 1977, *The Astrophysical Journal*, 217, 425
- Mathis J., Mezger P., Panagia N., 1983, *Astronomy and Astrophysics*, 128, 212
- McClure M., et al., 2012, *The Astrophysical Journal Letters*, 759, L10
- McClure M., et al., 2015, *The Astrophysical Journal*, 799, 162
- Min M., Dullemond C., Dominik C., de Koter A., Hovenier J., 2009, *Astronomy & Astrophysics*, 497, 155
- Min M., et al., 2016, *Astronomy & Astrophysics*, 593, A11
- Natta A., 1993, *The Astrophysical Journal*, 412, 761
- Noble J., Fraser H., Aikawa Y., Pontoppidan K., Sakon I., 2013, *The Astrophysical Journal*, 775, 85
- Nomura H., Millar T., 2005, *Astronomy & Astrophysics*, 438, 923
- Öberg K. I., 2009
- Öberg K. I., Garrod R. T., Van Dishoeck E. F., Linnartz H., 2009a, *Astronomy & Astrophysics*, 504, 891
- Öberg K. I., Fayolle E. C., Cuppen H. M., van Dishoeck E. F., Linnartz H., 2009b, *Astronomy & Astrophysics*, 505, 183
- Öberg K. I., Boogert A. A., Pontoppidan K. M., Van den Broek S., Van Dishoeck E. F., Bottinelli S., Blake G. A., Evans II N. J., 2011, *The Astrophysical Journal*, 740, 109
- Ossenkopf V., Henning T., 1994, *Astronomy and Astrophysics*, 291, 943
- Palumbo M., Strazzulla G., 1993, *Astronomy and Astrophysics*, 269, 568
- Palumbo M. E., Baratta G. A., Spinella F., 2006, *Memorie della Societa Astronomica Italiana Supplementi*, 9, 192
- Pontoppidan K. M., Dullemond C. P., Van Dishoeck E. F., Blake G. A., Boogert A. C., Evans II N. J., Kessler-Silacci J. E., Lahuis F., 2005, *The Astrophysical Journal*, 622, 463
- Pontoppidan K. M., et al., 2008, *The Astrophysical Journal*, 678, 1005
- Sandford S. A., Allamandola L. J., 1988, *Icarus*, 76, 201
- Sandford S., Allamandola L., Tielens A., Valero G., 1988, *The Astrophysical Journal*, 329, 498
- Schmitt B., Bollard P., Albert D., Garenne A., Gorbacheva M., Bonal L., Volcke P., and t. S. P. C., 2017, *SSHADE: "Solid Spectroscopy Hosting Architecture of Databases and Expertise"*, doi:10.26302/SSHADE, <https://www.sshade.eu/doi/10.26302/SSHADE>
- Semenov D., Wiebe D., 2011, *The Astrophysical Journal Supplement Series*, 196, 25
- Smith R. G., Sellgren K., Tokunaga A. T., 1989, *The Astrophysical Journal*, 344, 413

**Table A1.** Common disc parameters for the models

Property	Symbol	Value
Stellar Mass	$M_*$	$0.7 M_\odot$
Effective temperature	$T_*$	4000 K
Stellar luminosity	$L_*$	$1 L_\odot$
UV excess	$f_{UV}$	0.01
UV powerlaw index	$P_{UV}$	1.3
X-ray luminosity	$L_x$	$10^{30}$ erg/s
X-ray emission temperature	$T_x$	$2 \times 10^7$ K
Strength of interstellar UV	$\chi_{ISM}^{ISM}$	1
Strength of interstellar IR	$\chi_{IR}^{ISM}$	0
Cosmic ray $H_2$ ionisation rate	$\zeta_{CR}$	$1.7 \times 10^{-17} s^{-1}$
disc Mass	$M_{disc}$	$0.01 M_\odot$
Dust/gas mass ratio	$\delta$	0.01
Inner disc radius	$R_{in}$	0.07 au
Tapering-off radius	$R_{tap}$	100 au
Column density power index	$\epsilon$	1
Reference scale height	$H_g(100 \text{ au})$	10 au
Flaring power index	$\beta$	1.15
Minimum dust particle radius <sup>a</sup>	$a_{min}$	$0.05 \mu m$
Maximum dust particle radius <sup>a</sup>	$a_{max}$	$3000 \mu m$
Dust size dist. power index <sup>a</sup>	$a_{pow}$	3.5
Turbulent mixing parameter	$\alpha_{settle}$	0.01
Refractory dust composition	$Mg_{0.7}Fe_{0.3}SiO_3$	60%
	amorph. carbon	15%
	porosity	25%
PAH abundance rel. to ISM	$f_{PAH}$	0.01
Chemical heating efficiency	$\gamma^{chem}$	0.2
Distance to the observer	$d$	140 pc

<sup>(a)</sup> Parameters related to refractory dust grains.

The models use large DIANA chemical network composed of 235 species with 13 elements. The network is described in detail in Kamp et al. (2017).

- Terada H., Tokunaga A. T., 2017, *The Astrophysical Journal*, 834, 115
- Terada H., Tokunaga A. T., Kobayashi N., Takato N., Hayano Y., Takami H., 2007, *The Astrophysical Journal*, 667, 303
- Terada H., et al., 2012, *The Astronomical Journal*, 144, 175
- Tielens A., Tokunaga A., Geballe T., Baas F., 1991, *The Astrophysical Journal*, 381, 181
- Toon O. B., Ackerman T., 1981, *Applied Optics*, 20, 3657
- Vorhoeff A., et al., 2011, *Astronomy & Astrophysics*, 528, A91
- Voshchinnikov N., 2004, *ASPRv*, 12, 1
- Walsh C., Millar T. J., Nomura H., Herbst E., Weaver S. W., Aikawa Y., Laas J. C., Vasyunin A. I., 2014, *Astronomy & Astrophysics*, 563, A33
- Warren S. G., 1984, *Applied optics*, 23, 1206
- Warren S. G., 1986, *Applied optics*, 25, 2650
- Woitke P., Kamp I., Thi W.-F., 2009, *Astronomy & Astrophysics*, 501, 383
- Woitke P., et al., 2016, *Astronomy & Astrophysics*, 586, A103
- Zubko V., Mennella V., Colangeli L., Bussoletti E., 1996, *Monthly Notices of the Royal Astronomical Society*, 282, 1321

## APPENDIX A: DISC MODEL

Table A1 presents the disc properties considered for all the models presented in this paper. For more details regarding the parameters, meanings and their values, refer Woitke et al. (2009, 2016).

## APPENDIX B: COMPLEX FUNCTIONS FOR EFFICIENCY CALCULATIONS

The co-efficients  $a_n$  and  $b_n$  in Equation 6 are complex functions of refractive index and the size parameter of the particle. The following are the expressions that relate them (Krugel 2002).

$$a_n = \frac{\psi_n(x) \cdot \psi'_n(mx) - m\psi_n(mx) \cdot \psi'_n(x)}{\zeta_n(x) \cdot \psi'_n(mx) - m\psi_n(mx) \cdot \zeta'_n(x)} \quad (B1)$$

$$b_n = \frac{m\psi_n(x) \cdot \psi'_n(mx) - \psi_n(mx) \cdot \psi'_n(x)}{m\zeta_n(x) \cdot \psi'_n(mx) - \psi_n(mx) \cdot \zeta'_n(x)}$$

Further,

$$\psi_n(z) = z j_n(z)$$

$$\psi'_n(z) = z j_{n-1}(z) - n j_n(z) \quad (B2)$$

$$\zeta_n(z) = z [j_n(z) + i y_n(z)]$$

$$\zeta'_n(z) = z [j_{n-1}(z) + i y_{n-1}(z)] - n [j_n(z) + i y_n(z)]$$

The right hand side of the Equation B2 are calculated from recurrence relations (Equation B3)

$$j_n(z) = -j_{n-2}(z) + \frac{2n-1}{z} j_{n-1}(z)$$

$$y_n(z) = -y_{n-2}(z) + \frac{2n-1}{z} y_{n-1}(z) \quad (B3)$$

$$j_0(z) = \frac{\sin z}{z} \quad j_1(z) = \frac{\sin z}{z^2} - \frac{\cos z}{z}$$

$$y_0(z) = -\frac{\cos z}{z} \quad y_1(z) = -\frac{\cos z}{z^2} - \frac{\sin z}{z}$$

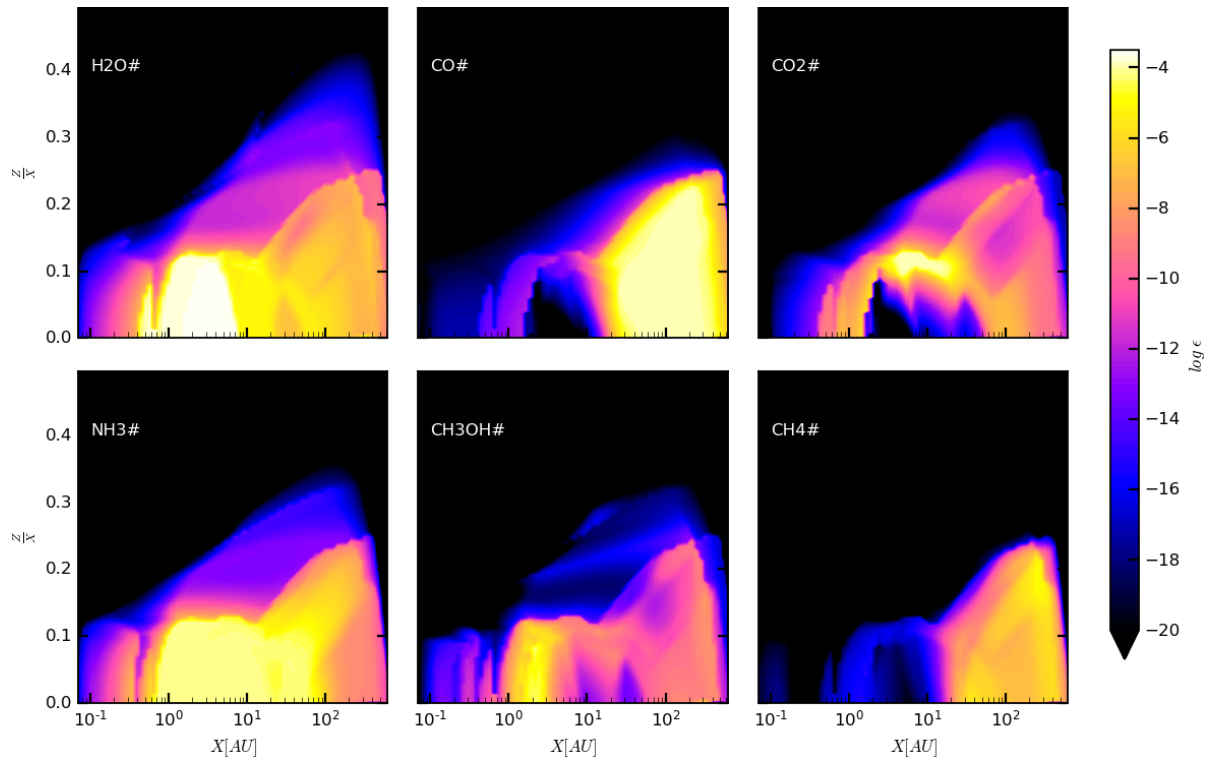
The asymmetry factor,  $g$ , which quantifies directional asymmetry in scattering is given by,

$$g = \frac{4}{x^2 Q^{sca}} \sum_{n=1}^{\infty} \left[ \frac{n(n+2)}{n+1} \text{Re}\{a_n^* a_{n+1} + b_n^* b_{n+1}\} + \frac{2n+1}{n(n+1)} \text{Re}\{a_n^* b_n\} \right] \quad (B4)$$

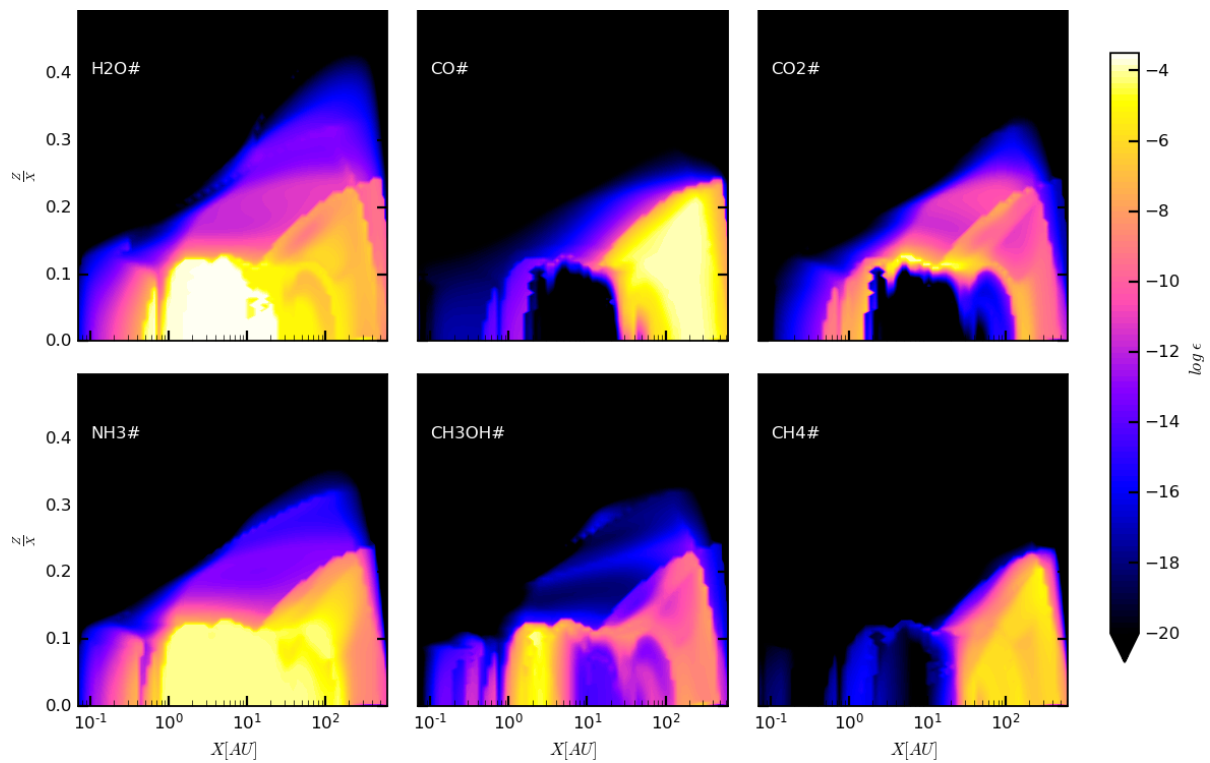
The terms  $a^*$ ,  $b^*$  are complex conjugates of  $a$  and  $b$ . These relations are solved numerically in ProDiMo using robust Mie routines. For well mixed grains, BHMIE (Bohren & Huffman 2008), MIEX (Voshchinnikov 2004), QMIE (Min et al. 2009) routines are used. Primarily, MIEX is used to make all the Mie calculations for the well mixed grains. In the case this routine fails, BHMIE is used, similarly QMIE is used if BHMIE fails. For the core-mantle Mie calculations DMilay (Dave 1968; Toon & Ackerman 1981) is used and if it fails, then CMIE routine (Cai 2019) is used. The complex refractive index of the well mixed grains are calculated using effective medium theory (Bruggeman 1935).

## APPENDIX C: ICE OPTICAL DATA

Refractive indices of six types of ice species are used which are tabulated in Table C1 and Figures C1 and C2. It is assumed that entire ice of one species is in same state, crystalline or amorphous. It should be noted that the ice optical data do not cover the entire spectrum ( $0.0912 \mu m - 10^4 \mu m$ ). Hence, the data has to be expanded extensively for all species to enable studying all the ice features.



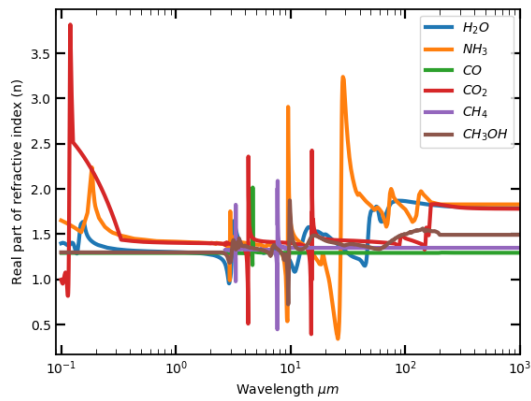
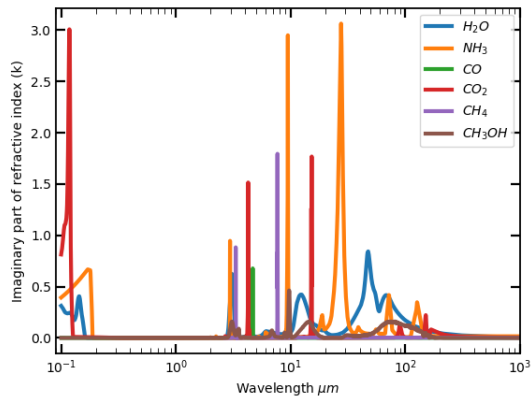
**Figure A1.** Typical ice distribution in the disc generated by ProDiMo without considering the position dependent opacities. Detailed disc properties are given in the Appendix A.



**Figure A2.** Typical ice distribution with ice opacities for model with constant ice thickness ( $n=0$ ). Detailed disc properties are given in the Appendix A.

**Table C1.** Ice and refractory species and refractive index data

Species	Data
H <sub>2</sub> O ice	Warren (1984)
NH <sub>3</sub> ice	Martonchik et al. (1984)
CO <sub>2</sub> ice	Warren (1986)
CO ice	Schmitt et al. (2017)
CH <sub>3</sub> OH ice	Hudgins et al. (1993)
CH <sub>4</sub> ice	Schmitt et al. (2017)
Amorphous Carbon	Zubko et al. (1996)
Silicate (Mg <sub>0.7</sub> Fe <sub>0.3</sub> SiO <sub>3</sub> )	Dorschner et al. (1995)

**Figure C1.** Real part of refractive indices of ice considered**Figure C2.** Imaginary part of the refractive indices of ices considered



## Chapter 3

# Conclusions and recommendations

This section discusses the conclusions drawn from the research presented in the journal paper (Chapter 2) and the recommendations for future work.

In this thesis, the effect of position-dependent ice opacities on the disc structure and appearance has been studied. The effect of ice accretion on the grain size distribution and composition are investigated. A generalized method of considering the dependence of ice thickness on the grain size due to dust coagulation or shattering is presented. It is found that the continuum opacity in the disc changes significantly and it strongly depends on the ice powerlaw or coagulation dominance factor which relates the ice thickness to grain size. Computationally efficient method of calculating the position-dependent ice opacities by interpolation between values from a pre-calculated Mie efficiency grid has been presented. This method has been implemented in ProDiMo and the optical appearance of the discs with ice opacities has been studied. The discs appear larger in absorption when ice opacities are considered. Dark lanes of absorption appear in the discs due to ice opacities. The position-dependent ice opacities do not change the physico-chemical structure of the disc significantly. Hence, the ices are not seen in either absorption or emission when observing the spectra from the entire disc. However, with better spatial resolutions, like those provided by NIRSpec instrument on board JWST, ice features can be observed by spectroscopy of the dark bands. The model also suggests that silhouette discs are better targets to observe ices in discs since the features are significantly enhanced with a background source. Based on these outcomes the following conclusions and recommendations are made.

### 3.1 Conclusions

Based on the journal paper in Chapter 2 and the research questions formulated in Chapter 1, conclusions are drawn and presented as answers to the research questions.

#### 1. How to implement position-dependent ice opacities in thermo-chemical disc models?

##### (a) What is the position-dependent amount and chemical composition of the ice in protoplanetary discs?

The ices in protoplanetary discs are generally dominated by H<sub>2</sub>O, yet several ice species are present in the discs. Based on the chemical network used for this work (see appendix of Chapter 2) and based on the availability of the optical data (complex refractive indices) in ProDiMo, H<sub>2</sub>O, NH<sub>3</sub>, CO, CO<sub>2</sub>, CH<sub>3</sub>OH and CH<sub>3</sub>OH ices are used to implement and study the effects of position-dependent ice opacities. The composition and abundance of ices depend on the local shielding and temperature. For the typical T Tauri disc considered in the paper, icy grains are generally dominated by H<sub>2</sub>O ice in regions within 10 au with significant amount of NH<sub>3</sub> ice. Regions beyond 10 au are generally dominated by CO ice. Yet, small regions dominated by CO<sub>2</sub> ice are present. Thus, the composition of the ice varies throughout the disc, depending on the local conditions and so does the opacity at each point.

##### (b) How does the thickness of the ice layers depend on grain size distribution?

The refractory grains can be covered by a constant thickness of ice independent of the grain size.

In regions where coagulation dominates, the ice distribution is such that the ice/refractory volume fraction is constant, in other words, the ice thickness is proportional to grain size. These two limiting cases are considered in the thesis. A generalised powerlaw definition is introduced for the dependence of ice thickness on the grain size. For the constant ice thickness case, the minimum grain size of the distribution increases. The increase in area due to ice accumulation is of several orders of magnitude larger for smaller grain sizes. The small grains are dominated by ices and larger grains by refractory materials. For the constant volume fraction case, both minimum and maximum grain sizes increase. The factor of increase in area is small yet uniform throughout the grain size. Since the volume fraction is conserved, the material composition of the icy grains remain same, independent of the grain size.

(c) **What are the effects of ice formation on continuum opacity?**

Due to ice formation, both composition and grain size change. These factors are directly related to opacity, thus, ice formation has significant effects on continuum opacity. For the case of constant ice thickness, the opacity at smaller wavelength is enhanced largely, dominated mainly scattering, and negligible change in larger wavelengths. The opacity plot shows that ice features are greatly enhanced. For the constant volume fraction case, the opacity increases uniformly at all wavelengths. The ice features are not as strong as for the previous case. This is mainly because of contribution of different grain sizes to the opacity, i.e. grains contribute to opacity at wavelength range close to their grain size. In the case of constant ice thickness, since most of the ice is in the smaller grains and since the smaller grains contribute significantly to the opacity on the shorter wavelengths, the ice features are significantly enhanced. However, for constant volume fraction case, the ice is largely accumulated in larger grains and these do not contribute much to the opacity at wavelengths where ice features are present. Hence, the ice features for constant volume fraction case is diminished.

(d) **How to calculate the opacities of the icy grains in a computationally efficient way?**

To calculate the opacities based on the local ice composition and abundance at each grid point in the disc, the computational power requirement is high. Instead of performing Mie efficiency calculations at every grid point in the disc, a pre-calculated Mie efficiency matrix is generated and interpolation is done between the values of this matrix to obtain the local Mie efficiency values. This matrix mainly has 4 dimensions: number of ice thicknesses, number of ice species, number of ice power laws and number of bare grain material compositions. This matrix is first calculated using effective medium and Mie theories. Based on the selected bare grain composition and ice power law, an ice volume fraction weighted sum in the ice species dimension and a log interpolation in ice thickness dimension are performed. This reduces the computational time by  $O(\text{Spatial disc grid size}/\text{Mie efficiency matrix grid size})$  for the position-dependent opacity computation, which is  $O(\frac{80 \times 80}{7 \times 8}) \approx O(10^2)$  for the models considered in this work.

## 2. What are the effects of the opacities of ice-coated grains in protoplanetary discs?

(a) **What is the effect of position-dependent ice opacities on the physical and chemical structure of the disc?**

The ice opacities increase the optical extinction in the midplane of the disc significantly compared to bare grain opacities (for example, vertical extinction increases by a factor of more than 10 at 10 au in the midplane). The surface temperature of the disc becomes cooler, however the change in temperature is small throughout the disc. The interior temperature of the disc is largely determined by the scattering and re-emission of the stellar radiation by the surface layer. Since, ices are present only in cold and shielded regions of the disc, the dust in the surface layers are composed of only the refractory material and no ice. Thus the optical properties of the surface layer does not change and thus the physico-chemical structure of the disc remain almost the same as with bare grain opacities.

(b) **How do the position-dependent ice opacities change the optical appearance of protoplanetary discs from optical to millimeter wavelengths?**

The spectral energy distribution (SED) mostly remains unaffected by the position-dependent ice opacities. This is a consequence of the temperature of the disc being largely unchanged. In other words, the temperature of the regions from where the observed radiation is emitted does not change. At high inclination, example at  $90^\circ$ , the flux at shorter wavelengths is smaller by an

order of magnitude. This is because of the larger optical depth and column densities of ice in the midplane at higher inclinations. Further, the model predicts that it is close to impossible to observe ice emission or absorption features in the SED. This is because ices form in the midplane of the disc which are optically thick. The regions outside the midplane which contribute to the SED do not contain ices. This result also shows that the previously observed ice features in the SED are either outside the disc, for example in the envelope, or some dynamical process exists that can transport ice to the surface layer of the disc, for example comets and turbulence. The discs appear larger in absorption when position-dependent ice opacities are included. Particularly at wavelength corresponding to ice features, dark lanes appear in the disc images. The width and darkness of the lane depends on the relation between ice thickness and grain size. The bands become darker for constant ice thickness model compared to the constant volume fraction model. This is a direct consequence of the different opacities these models have. However, these bands appear due to the ices in the outer disc regions and are not affected by the ice power law in the midplane.

(c) **What are the predictions of observational ice-features for future space-borne telescopes such as JWST and SPICA?**

The position-dependent ice opacity model predicts that the total disc flux does not reveal ice features in a typical T Tauri disc. However, with instruments that have high spatial resolution like NIRSpec in JWST, ices can be observed and analysed by spectroscopy of the dark lanes. Further, the model predicts that the features are significantly strong for silhouette discs, making them better observational targets for future observations.

## 3.2 Recommendations

The implementation of the position-dependent opacity computation has expanded the scope of using ProDiMo to model protoplanetary discs. The possible improvements that can be made to the position-dependent code and the application of the code is discussed below.

- With telescopes like JWST and SPICA soon to be launched, we are entering an era where observations can probe the upper midplane of protoplanetary discs. Hence, the current thermo-chemical models can be tuned, verified and validated by the observations. Such improvements will allow determining constraints on various processes and properties such as coagulation of dust and its composition. This improves the accuracy of predicting and analysing the observational data as well as identifying the promising objects.
- The presented position-dependent ice opacities are computed from a set of fixed optical constants for each material, where the local abundance and chemical composition of the ice depend on local temperature and shielding conditions. However, the model now also offers an opportunity to consider temperature-dependent optical constants for a single material (both for ices and bare grain materials). For example, Maaskant et al. (2015) studied the temperature dependent  $69\ \mu\text{m}$  feature of forsterite in Herbig Ae discs with Herschel. Water ice has distinct complex refractive indices for amorphous and crystalline form. Considering for example only amorphous  $\text{H}_2\text{O}$  ice, the refractive indices change with temperature (Hudgins et al., 1993). Since, optical data for each temperature of a certain ice can be considered as a separate ice species, temperature dependence can be implemented by considering the ice optical data in the right temperature range while interpolating in the species dimension.
- In the current model the effect of ice formation on opacity and its radiative feedback on the disc have been studied. This can be improved in the future by communicating the changes in size distribution and grain composition to the rest of the disc code. Current dust settling code in ProDiMo considers only the refractory grains in the disc. The changes in size and mass density of the grains due to ice accretion will affect dust settling. This can cause displacement of ices in the disc. This will change the local chemical composition which affects both the local opacity and chemistry.
- Dust coagulation and shattering models can be implemented to improve position-dependent opacity estimation. Based on the outcome of coagulation/shattering code, the relation between ice thickness and grain size can be locally determined which further improves the accuracy of position-dependent opacity computation. These results can be interfaced with opacity module of the disc model easily,

since the opacity grid has ice power law ( $n$  in  $\Delta a = t \cdot a^n$ , where  $a$  is the bare grain size,  $t$  and  $n$  are ice power law factors that account for the ice abundance and dominance of coagulation or shattering of grains) as one of the dimensions. The ice power law can strongly change the opacity in the disc as discussed in the conclusion. Further, such models can be used to study whether ice accumulation on the grain happen before or after the grains coagulate, because, both of these conditions yield a different bare grain and ice distribution.

# Appendix A

## Position-dependent opacity implementation in ProDiMo

### A.1 ProDiMo flowchart

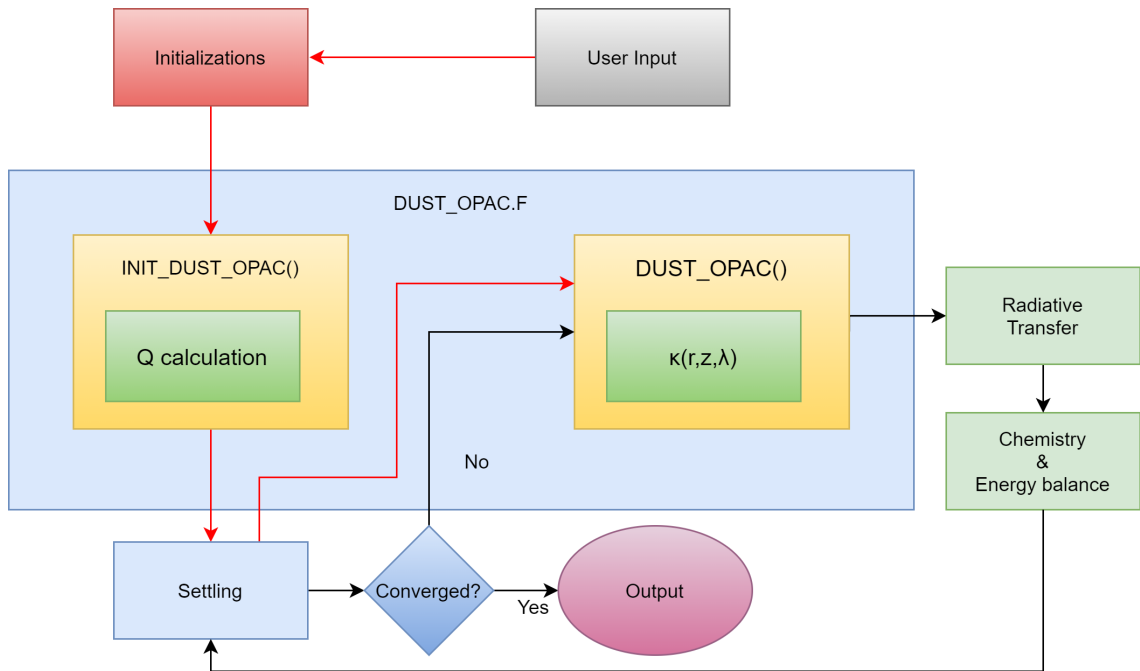


Figure A.1: ProDiMo flowchart prior to position-dependent opacities implementation, red lines indicate flow path during initialization stage, black lines indicate the program flow during the main iterations

Figures A.1 and A.2 show the structure of F90 code structure of ProDiMo prior to and after implementation of position-dependent opacities. In both figures, the red lines indicate the flow of control during the initialization stage or first iteration of the code. These flow lines can be neglected once the flow enters the main iteration (indicated by black lines). The code reads the input files provided by the user and starts the initialization of the disc model parameters and structure. This includes allocating variables and their values, defining the column density profile, dust distribution bins, etc. Prior to the implementation of position-dependent opacity computation, the code would enter `INIT_DUST_OPAC()` subroutine, in which the grain size distribution is initialised, the complex refractive indices of dust material is read, and the scattering, absorption and extinction efficiencies are calculated. This subroutine is called only once in the entire run. Then settling subroutine solves for dust settling in the disc (based on Dubrulle et al. (1995)). This produces the number density of different grain sizes at each disc grid point. Based on these number densities and efficiencies, the

opacity at each grid point ( $\kappa(r, z, \lambda)$ ,  $r$  is the radial distance from disc axis,  $z$  is the height from midplane and  $\lambda$  is the wavelength) of the disc is calculated in `DUST_OPAC()` subroutine. It should be noted that at this point the code has entered the main iteration loop and flow of control follows the black line. This opacity data is then used in the radiative transfer module. This module computes the 3D the radiation field and 2D dust temperature structure. Then the chemistry is solved, consistently with the gas heating/cooling balance, based on the local radiation field, which results in distribution of chemical species and the gas temperature in the disc. The flow is passed to the settling module to calculate the dust structure of the disc. Convergence is evaluated at the end of each iteration. Here the pressure structure or the gas abundance values at each grid point is compared to the previous iteration also taking into account the number of points where there is a rapid change of values above or below a certain range. If the convergence value is above a certain threshold then the solution has not converged and continues the iterations following the black lines in Fig. A.1. Each subsequent iteration starts by computing again the dust opacity, which depends on the dust settling. Once the disc model is converged, the code produces several output files containing the physico-chemical disc structure and observables. If convergence has not been reached, then the code enters the next iteration.

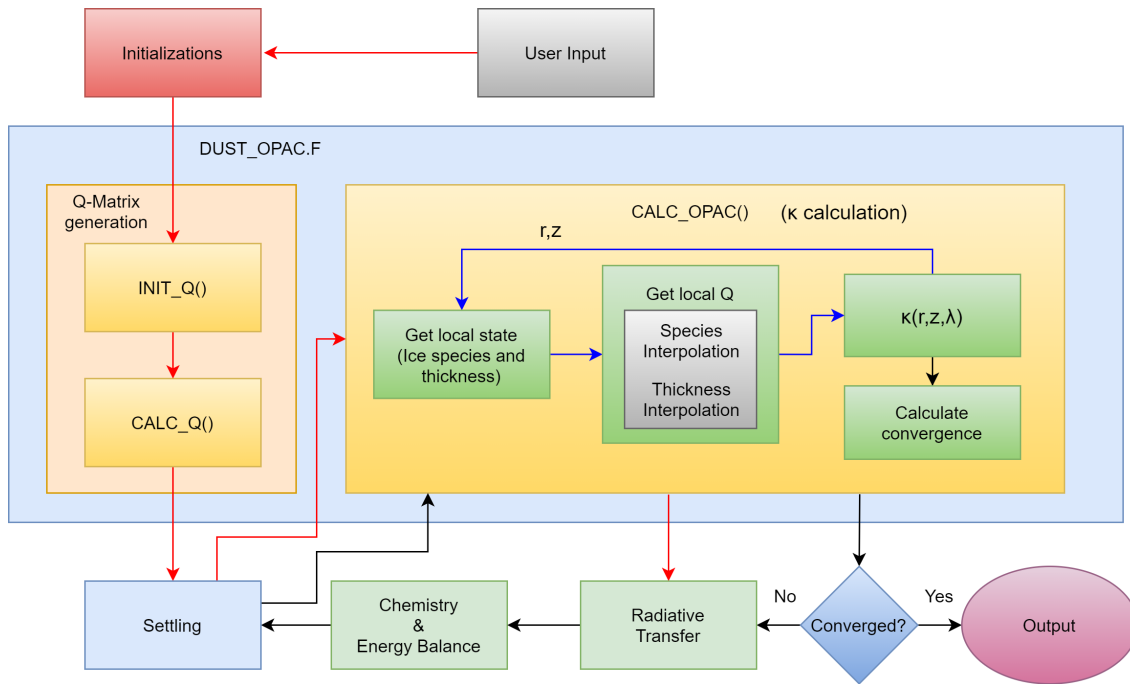


Figure A.2: ProDiMo flowchart with position-dependent opacities implemented, red lines indicate flow path during initialization stage, black lines indicate the program flow during the main iterations and blue lines indicate the flow loop within the `CALC_OPAC()` subroutine

With the position-dependent opacities implementation (Fig. A.2), the subroutines in `DUST_OPAC.F` are re-written and the flow is changed as well. In the user input stage, the user can choose to use the new implementation and define the ice opacity grid size, which includes the selection of ice species to be considered, the number of ice thicknesses to be considered, the ice power law, and the choice of refractory grain materials. After the initialization of the physical disc structure, it enters `INIT_Q()` subroutine. In this subroutine, the refractive indices of refractory and ice materials are read, the Mie efficiency grid/matrix is initialized with the shape and allocation of memory. A number of checks are performed to affirm the ice data is available and those species are considered in the chemistry module of ProDiMo. Then, it enters `CALC_Q()` subroutine, where the Mie efficiency matrix is populated with data. Each grid point represents a combination of ice grain conditions. For example: the ice species, ice thickness and power law coefficients and bare grain composition. The subroutine also checks if pre-calculated data matching the current disc model conditions is available in a local file, and takes data from that file if available. If it is not available, a file is created in the end of the subroutine. The dust settling module, then, determines the dust distribution in the disc. Then the flow enters `CALC_OPAC()` subroutine which is where the position-dependent ice opacities are computed. The code goes through each point in the disc spatial grid, and fetches the local abundances of the ice species selected by the user, upon which the ice thickness is calculated. The opacities are then calculated by interpolation considering the closest pre-computed results for ice abundances and ice thickness as discussed in

Chapter 2. These interpolated  $Q$ -values are then used along with the number density of dust grains generated by settling module, to calculate the mass opacity at that grid point. These steps are performed for each grid point indicated by the blue line in Fig. A.2. This opacity data is then passed to the radiative transfer model to determine the radiation field and dust temperature in the disc. At this point the code has entered the main iteration loop and flow of control follows the black line. The chemistry and energy balance module is then run and subsequently the dust structure in the disc is calculated by the dust settling module. With the updated chemical abundances, particularly based on the new ice abundance at each grid point, the new position-dependent opacities are calculated. These opacities are then compared to the position-dependent opacities from the previous iteration to evaluate opacity convergence. After this, disc convergence (now it also includes convergence value passed on from opacity subroutine) is evaluated and either the output is produced or the flow enters the next iteration depending on whether the model has converged.

The opacity convergence is evaluated as:

$$\text{Cumulative Relative Error} = \sum_{r,z,\lambda} \left| \frac{\kappa_{new}(r,z,\lambda) - \kappa_{old}(r,z,\lambda)}{\kappa_{old}(r,z,\lambda)} \right| \quad (\text{A.1})$$

$$\text{Convergence} = \frac{\text{Cumulative Relative Error}}{N_r \times N_z \times N_\lambda} \quad (\text{A.2})$$

where,  $\kappa$  is the mass opacity,  $N_r$ ,  $N_z$  and  $N_\lambda$  are the size of grid points in spatial ( $r$ ,  $z$ ) and wavelength ( $\lambda$ ) dimensions respectively. If this convergence value is below the user defined convergence tolerance, then the opacity is assumed to be converged. It should be noted that with the position-dependent opacity implementation, the code needs a minimum of two iterations to reach convergence (opacity). This is because, when the disc structure is initialized there are no ices present in the disc and hence the opacities are based on the refractory material only. However, once the chemistry is solved in the first iteration, ice data will be available and then the ice opacities can be estimated.

## A.2 Ice thickness calculation

The chemistry module in ProDiMo solves for chemical equilibrium of the disc. This solution provides chemical abundances of the various species considered which includes ices. The chemistry module used in this work is the large DIANA network (Kamp et al., 2017). This reaction network considers a total of 235 chemical species composed of 13 elements: H, He, C, N, O, Ne, Na, Mg, Si, S, Ar, Fe and PAH (though PAH is a molecule, here it is considered as an element for chemical reactions). The reaction rates are mainly based on UMIST2012 database. A total of 4835 chemical reactions are considered. 137 photo reactions which include photo dissociation and photo ionisation reactions are considered. Some reactions (mostly photo dissociation reactions) not in UMIST database are taken from Heays et al. (2017). The photo dissociation and ionization cross sections are taken from Heays et al. (2017), van Dishoeck et al. (2006). Three body reactions are taken from UMIST2006. PAH used here is circumcoronene ( $C_{58}H_{18}$ ), with mass 666.74 atomic mass units per macromolecule, radius  $4.87 \times 10^{-8}$  cm and adsorption energy of 34380 K (Kamp et al., 2017). The 235 chemical species include both gas and ice phases, particularly 64 ice species. The adsorption energies for ices are mainly based on Garrod and Herbst (2006). The details of chemical setup are discussed in Kamp et al. (2017). The ice chemistry is only based on accretion and desorption of ices and grain surface chemistry is not considered. The chemical abundance of ices at each grid point is provided by the solution of this setup. Hence, in the initialization stage of the code, the code checks whether the ice selected by the user is present in the chemical network. Based on these chemical abundances of species selected by the user, the ice composition and volume of ice at each grid point is calculated. The adsorption energies, refractive indices wavelength range, mass densities and references to the values for the ices used in this thesis are reported in Tab. A.1. For the ice thickness dimension of the opacity grid, a number of ice thicknesses between zero to maximum are considered. The maximum thickness is based on the maximum volume ( $V_{max}$ ) of ice that can form in the disc. For  $V_{max}$ , it is assumed that all the available oxygen forms  $H_2O$  ice, carbon forms  $CH_4$  ice and nitrogen  $NH_3$  ice  $V_{max}$  at each grid point. Hence,  $V_{max}$  is assumed to be:

$$V_{max} = n_H \cdot \epsilon_O \cdot V_{H_2O} + n_H \cdot \epsilon_C \cdot V_{CH_4} + n_H \cdot \epsilon_N \cdot V_{NH_3} \quad (\text{A.3})$$

$n_H$  is the number density of hydrogen nuclei [ $\text{cm}^{-3}$ ],  $\epsilon_k$  is the elemental abundance [number of nuclei of element  $k$ /H-nucleus],  $V$  is the volume of one molecule of that ice species [ $\text{cm}^3$ ]. For example, if the user

Ice	Adsorption Energy (K)	Source	Refractive index wavelength range ( $\mu\text{m}$ )	Mass density $\text{g}/\text{cm}^3$	Reference
H <sub>2</sub> O	5534.0	Brown and Bolina (2007)	0.1-10 <sup>3</sup>	0.92	Warren (1984)
NH <sub>3</sub>	4800.0	Collings et al. (2004)	0.1-10 <sup>3</sup>	0.817	Martonchik et al. (1984)
CO	1150.0	Collings et al. (2004)	0.1-10 <sup>3</sup>	0.791	Schmitt et al. (2017)
CO <sub>2</sub>	2990.0	Theys et al. (2013)	0.1-10 <sup>3</sup>	1.562	Warren (1984)
CH <sub>4</sub>	1090.0	Herrero et al. (2010)	2.7-10	0.44	Schmitt et al. (2017)
CH <sub>3</sub> OH	4930.0	Brown and Bolina (2007)	2.5-200	0.63	Hudgins et al. (1993)

Table A.1: Adsorption energies, wavelength range of refractive indices and mass densities of the ices considered in this thesis. The optical range outside the given range if needed is taken as constant towards shorter wavelengths and is interpolated in log scale for the longer wavelengths.

specifies the grid dimension for thickness as 8, then the ice volumes considered are 0,  $V_{max}$  and 6 volumes equally space between 0,  $V_{max}$  in log scale.

The thickness of the ice depends on the total ice volume available, the grain size distribution and the relation between the ice thickness to the grain size. Equation of volume conservation can be written as discussed in Chapter 2:

$$\begin{aligned}
 n_d \int_{a_{min}}^{a_{max}} \frac{4}{3} \pi (a + \Delta a)^3 f(a) da &= V_I + n_d \int_{a_{min}}^{a_{max}} \frac{4}{3} \pi a^3 f(a) da \\
 n_d \int_{a_{min}}^{a_{max}} \frac{4}{3} \pi (a + t \cdot a^n)^3 f(a) da &= V_I + n_d \int_{a_{min}}^{a_{max}} \frac{4}{3} \pi a^3 f(a) da \\
 F &= V_{IG} - V_I - V_{BG} = 0 \\
 F &= n_d \frac{4\pi}{3} \sum_{i=i_{min}}^{i_{max}} (a_i + t a_i^n)^3 f_i da_i - V_I - n_d \frac{4\pi}{3} \sum_{i=i_{min}}^{i_{max}} a_i^3 f_i da_i = 0
 \end{aligned} \tag{A.4}$$

$n_d$  is the number density of bare grains [ $\text{cm}^{-3}$ ],  $f(a)$  is the normalized bare grain size distribution after settling [ $\text{cm}^{-1}$ ],  $a$  is the bare grain size [cm],  $a_{min}$  and  $a_{max}$  are the minimum and maximum grain sizes,  $t$  and  $n$  are the ice-grain size relation coefficients as described in Chapter 2,  $V_I$ ,  $V_{IG}$ ,  $V_{BG}$  are the volumes of pure ice, ice cover grains, bare grains per unit volume of space respectively. The continuous size distribution is implemented in the code using size bins represented by  $a_i$ ,  $f_i$ ,  $i_{min}$  and  $i_{max}$ . The Eq. (A.4) contains only 1 unknown,  $t$ , since  $n$  is fixed for each such calculation. This is solved using Newton-Raphson method by minimising the function  $F$  against  $t$  in Equation A.4. To make the first estimate of  $t$ , Equation A.4 can be expanded as:

$$\begin{aligned}
 F &= t^3 \left[ n_d \sum_{i=i_{min}}^{i_{max}} f_i a_i^{3n} \Delta a_i \right] + t^2 \left[ 3n_d \sum_{i=i_{min}}^{i_{max}} f_i a_i^{2n+1} \Delta a_i \right] + t \left[ 3n_d \sum_{i=i_{min}}^{i_{max}} a_i^{n+2} f_i \Delta a_i \right] - V_I \frac{3}{4\pi} = 0 \\
 F &= At^3 + Bt^2 + Ct + D = 0
 \end{aligned} \tag{A.5}$$

$$A = n_d \sum_{i=i_{min}}^{i_{max}} f_i a_i^{3n} \Delta a_i, \quad B = 3n_d \sum_{i=i_{min}}^{i_{max}} f_i a_i^{2n+1} \Delta a_i, \quad C = 3n_d \sum_{i=i_{min}}^{i_{max}} a_i^{n+2} f_i \Delta a_i, \quad D = -V_I \frac{3}{4\pi}$$

Neglecting the highest order term  $At^3$ , the first estimate is taken as:

$$t = \frac{-C + \sqrt{C^2 - 4 \cdot B \cdot D}}{2 \cdot B} \tag{A.6}$$

If the function gives value less than  $10^{-12}$  [ $\text{cm}^{1-n}$ ] then it is assumed to be converged. If it fails to converge in 100 iterations then the ice thickness is take as zero, or in other words, bare grains are considered. Eq. A.3 expresses the maximum volume of ice considered in the Mie efficiency matrix. However, the volume of ice at any grid point for local Mie calculation is obtained as shown in Eq. A.7.

$$V = n_{H_2O} \cdot V_{H_2O} + n_{NH_3} \cdot V_{NH_3} + n_{CO} \cdot V_{CO} + n_{CO_2} \cdot V_{CO_2} + n_{CH_3OH} \cdot V_{CH_3OH} + n_{CH_4} \cdot V_{CH_4} \tag{A.7}$$

$n_k$  is the abundance of ice species  $k$  [ $\text{cm}^{-3}$ ],  $V_k$  is the volume of one molecule of ice species  $k$  [ $\text{cm}^3$ ] and  $V$  is the total ice volume per unit volume of space at any given grid point of the disc.

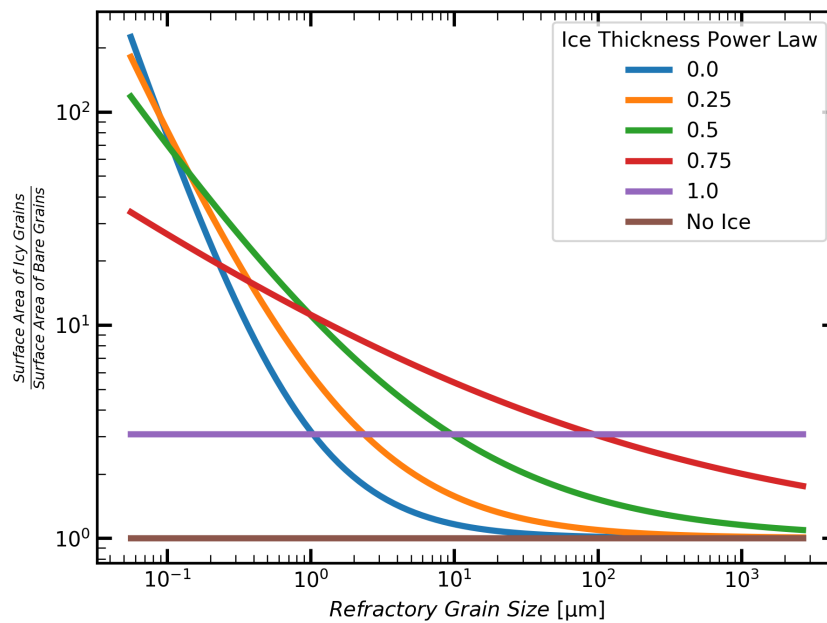


Figure A.3: Relative change of surface area of dust due to different ice accretion powerlaws. The grain size distribution and ice abundances are same as Fig. 1 in journal paper in Chapter 2

Figure A.3 shows the change in surface area due to ice accretion on bare grains for various ice power laws (the size distribution and ice abundances are same as in Figure 1 of Chapter 2). The change in surface area is more towards the smaller grain sizes and negligible for larger grains for powerlaws 0, 0.25, 0.5. As the powerlaw reaches close to 1, the change in area becomes uniform across the distribution. Thus for a constant ice thickness model, the surface area is not only dominated by smaller grains, but is increased by several orders of magnitude compared to bare grains. The effect of this can be seen as a peak in opacity at shorter wavelengths in Figure 5F (Chapter 2).

### A.3 Opacity grid

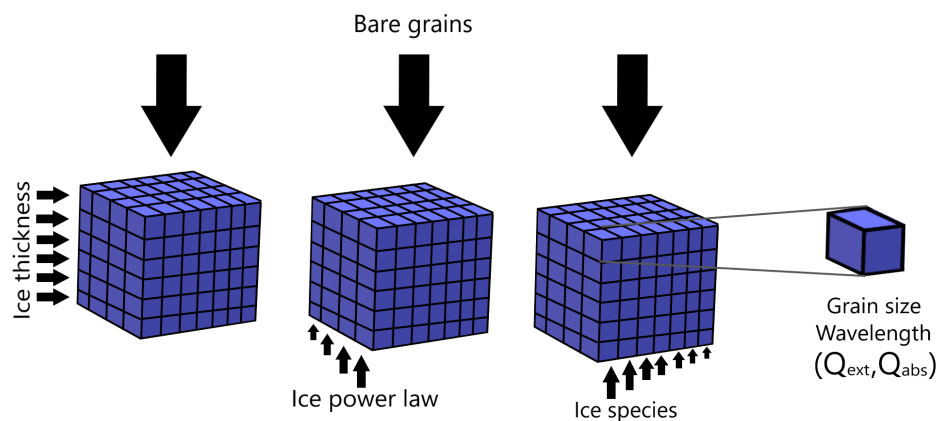


Figure A.4: Representation of the opacity grid implemented in ProDiMo

Figure A.4 provides the visualisation of the multidimensional  $Q$ -matrix implemented in ProDiMo for position-dependent opacity calculations. Primarily, there are 4 dimensions: ice thickness, ice species, ice power law,

bare grains. Each grid point in this setup is itself a 3 dimensional matrix of opacity efficiencies ( $Q_{ext}(a, \lambda)$ ,  $Q_{abs}(a, \lambda)$ ), making the grid structure a 7 dimensional matrix. However, for this thesis, only one type of bare grain composition is considered and one ice power law for each model (except for model 4 in Figure 6, Chapter 2, which has 2 ice power laws).

The grid size used for all the models in this thesis (except model 4) is (ice thickness, ice species, ice power law, bare grains) = (8,7,1,1), (grain size bins, wavelengths,Q) = (100,1000,2). For model 4, (ice thickness, ice species, ice power law, bare grains) = (8,7,2,1).

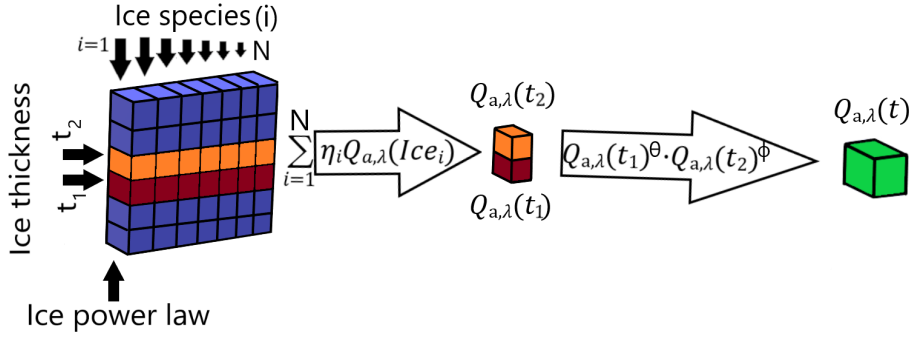


Figure A.5: Navigation in the grid during interpolation

To obtain the local opacity efficiencies,  $Q_{a,\lambda}(t)$ , the code first fetches the local abundances of ice species from the chemistry module. Based on these abundances, the ice volume fraction ( $\eta$ ) of each species and the total ice volume is calculated. Based on the local grain size distribution and the ice power law, the ice layer thickness  $t$  is calculated as discussed in Appendix A.2. The closest two thickness values ( $t_1$ ,  $t_2$ ) to the local thickness corresponding to the local ice power law is identified (Fig. A.5). From the opacity grid, weighted summation of opacities of different ice species is done based on volume fraction calculated for both the identified thicknesses to obtain  $Q_{a,\lambda}(t_1)$  and  $Q_{a,\lambda}(t_2)$ . Finally, log interpolation is done to estimate  $Q_{a,\lambda}(t)$ .

## Appendix B

# Interpreting the ProDiMo output

ProDiMo provides several output data files which contain the Spectral Energy Distribution (SED), the opacity, the radial and vertical visual extinction, the chemical abundances, continuum images (intensity maps), etc., of which the important results are presented in the journal paper in Chapter 2. The image data output by ProDiMo provides the spectral intensity at a given inclination of the disc in spatial and spectral dimensions, i.e.,  $I_\nu(x, y, \lambda)$ , where  $x, y$  are the image coordinates in [au] at given distance and  $\lambda$  is the wavelength. The spectral grid points are equally spaced in log scale. However, the spatial grid points are not linearly spaced in  $x, y$ . The intensity [erg/cm<sup>2</sup>/s/Hz/sr] data is converted to flux,  $\nu F_\nu$  [W/m<sup>2</sup>] which allows to obtain a spectra from parts of the image, as function of wavelength, ranging from 0.1  $\mu\text{m}$  to 10<sup>3</sup>  $\mu\text{m}$ . Such spectra, allows for a comparison of the model data with spectroscopic performance of instruments such as NIRSpec on JWST.

Intensity at a point is the energy ( $dE$ ) passing through a solid angle  $d\Omega$  per unit time  $dt$  in the spectral range  $d\nu$  in an infinitesimal inclined area  $dA \cos\theta$ .

$$I_\nu = \frac{dE}{d\nu d\Omega dt dA \cos\theta} \quad (\text{B.1})$$

$$I_\nu = I_\nu(\theta, \phi)$$

Flux from a source can be obtained by integrating the intensity over the solid angle of the source. Hence,

$$F_\nu = \int_{source} I_\nu(\theta, \phi) d\Omega \quad (\text{B.2})$$

As the data output by ProDiMo is not regularly spaced in linear scale, the data is interpolated onto a regular spatial grid using `interpolate.griddata()` from the SciPy library in python. This uses piecewise cubic interpolation. The grid resolution of 1.5 AU  $\times$  1.5 AU spatially and 300 wavelength bins are used, i.e., for an image data of 300 AU  $\times$  300 AU, the data is interpolated onto a 200  $\times$  200  $\times$  300 grid. This interpolation is done because it is easier to implement Equation B.2 on a regularly spaced grid. The integration now becomes,

$$F_\nu = \sum_{x,y} \left( \frac{I_\nu \cdot \Delta A_{x,y}}{d^2} \right) \quad (\text{B.3})$$

where,  $x, y$  are the spatial grid points,  $\Delta A$  is the element area and  $d$  is the distance from the observer. Based on the angular resolution of the instruments, this grid range for integration is determined. For example, for a disc at a distance of 140 pc from the observer, with an angular resolution of 0.2''  $\times$  0.4'', corresponding to NIRSpec microshutter mode, the pixel resolution would be approximately 28 AU  $\times$  65 AU on the disc image. Hence, the flux seen by the pixel is,

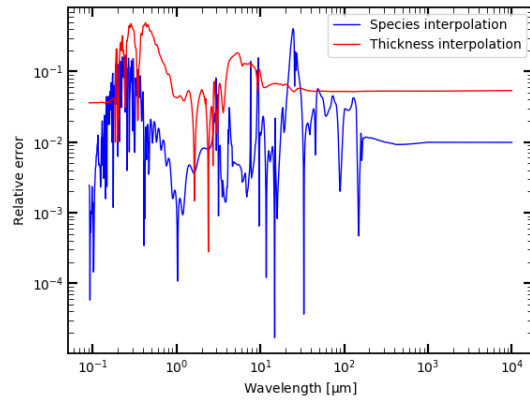
$$F_\nu(pixel_i) = \sum_{x,y} \left( \frac{I_\nu \cdot \Delta a_{x,y}}{d^2} \right), \quad x, y \in pixel_i \quad (\text{B.4})$$



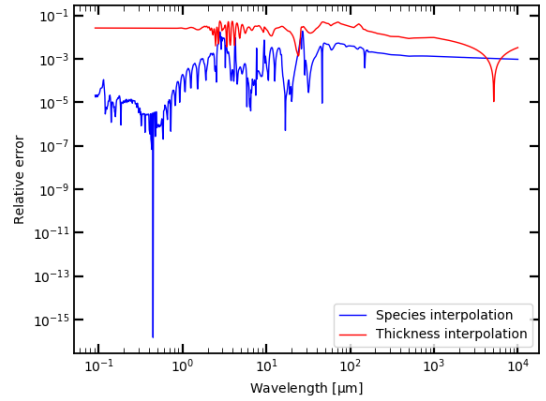
# Appendix C

## Verification and Validation

The interpolation method introduced in Chapter 2 has been verified by comparing the efficiency values obtained by interpolation in the Mie efficiency matrix with the values from Mie computations with the actual ice composition and thickness. Fig. C.1 and C.2 show the relative error between the actual and interpolated Mie efficiency values for different grain sizes. The interpolation is accurate, however for small grain size at short wavelengths between  $0.1 \mu\text{m}$  and  $1 \mu\text{m}$  the error is comparatively higher for independent of ice composition and ice thickness.

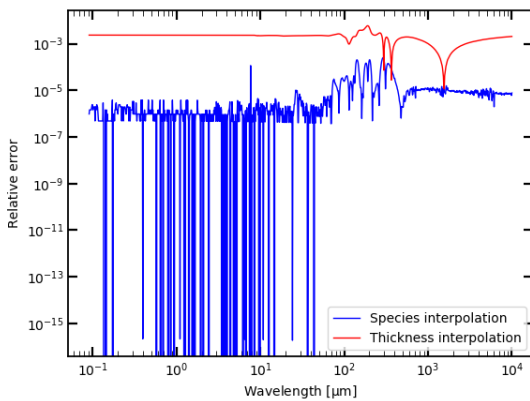


(a) Grain size =  $0.0559 \mu\text{m}$

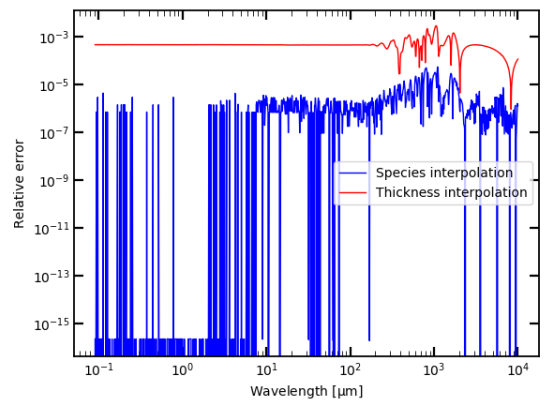


(b) Grain size =  $3.813 \mu\text{m}$

Figure C.1: Relative error in performing interpolation of Mie efficiencies. Ice thickness =  $0.515 \mu\text{m}$ , ice is composed of  $\text{H}_2\text{O}$ ,  $\text{NH}_3$ ,  $\text{CO}$ ,  $\text{CO}_2$ ,  $\text{CH}_4$ ,  $\text{CH}_3\text{OH}$  in ratio  $0.16:0.16:0.16:0.2:0.16:0.16$  with 20% of porosity



(a) Grain size =  $54.905 \mu\text{m}$



(b) Grain size =  $290.786 \mu\text{m}$

Figure C.2: Relative error in performing interpolation of Mie efficiencies. Ice thickness =  $0.515 \mu\text{m}$ , ice is composed of  $\text{H}_2\text{O}$ ,  $\text{NH}_3$ ,  $\text{CO}$ ,  $\text{CO}_2$ ,  $\text{CH}_4$ ,  $\text{CH}_3\text{OH}$  in ratio  $0.16:0.16:0.16:0.2:0.16:0.16$  with 20% of porosity

This is because, at wavelengths close to particle size, artifacts due to resonance between wavelength of radiation and grain size. However, these artifacts are automatically diminished when a grain size distribution is considered.

Figures C.1 and C.2 show the relative errors for different grain sizes. The relative error is comparatively higher at wavelengths close to the grain size. The overall magnitude of the relative error decreases with increase in bare grain size. Further, this interpolation has been tested for 72 different ice composition across 7 ice thicknesses for multiple bare grain sizes. The relative errors remain in the same range for all the ice compositions. Figure C.3 shows the relative error for different ice thicknesses. The behaviour is same as explained before in the wavelength range close to grain size. However, the overall relative error increases with decreasing ice thickness. The interpolation codes have been independently implemented in Fortran and Matlab. Both the codes produce the same results. Generally, the main source of error is the thickness interpolation. It should be noted that the grain size distribution used in the thesis has significantly large number of small grains and few large grains. Figures C.1 and C.2 indicate that the errors are larger for smaller grains. Although the errors are small, the small grains contribute to most of the error arising from these interpolations. However, the propagation of this error in the code is not investigated in this work.

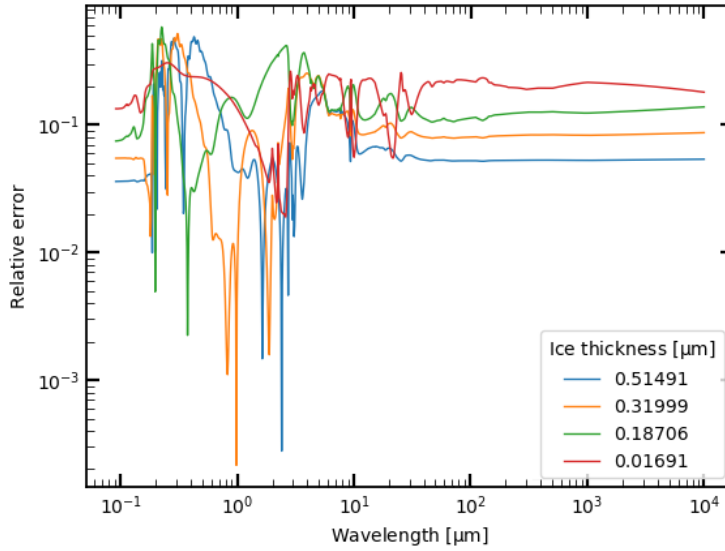


Figure C.3: Relative error in performing interpolation of Mie efficiencies. Bare grain size =  $0.0559 \mu\text{m}$ , ice is composed of  $\text{H}_2\text{O}$ ,  $\text{NH}_3$ ,  $\text{CO}$ ,  $\text{CO}_2$ ,  $\text{CH}_4$ ,  $\text{CH}_3\text{OH}$  in ratio 0.16:0.16:0.16:0.16:0.16:0.2 with 20% of porosity

After the position-dependent opacity calculation method has been implemented in ProDiMo, the code has been checked for integrity with rest of the code modules. This is done so that the new implementation does not break the code or produce different output for the inputs that do not consider position-dependent opacities, such as molecular cloud and envelope models. This ensures that the end user of ProDiMo, who is not using position-dependent opacities, is not affected by the new implementation. These tests have been done by the automatic test routine hosted by ProDiMo development team. This includes 17 automatic tests for different objects (such as molecular clouds, envelopes and discs) and input options (such as including X-ray radiative transfer, using fixed surface density model, multiple zoned disc model). The latest test results can be access at: <https://www.astro.rug.nl/~rab/punit.html>

# Bibliography

- Andrews, S. M. and Williams, J. P. (2005). Circumstellar dust disks in taurus-auriga: the submillimeter perspective. *The Astrophysical Journal*, 631(2):1134.
- Andrews, S. M. and Williams, J. P. (2007). A submillimeter view of circumstellar dust disks in  $\rho$  ophiuchi. *The Astrophysical Journal*, 671(2):1800.
- Armitage, P. J. (2010). *Astrophysics of planet formation*. Cambridge University Press.
- Brown, W. A. and Bolina, A. S. (2007). Fundamental data on the desorption of pure interstellar ices. *Monthly Notices of the Royal Astronomical Society*, 374(3):1006–1014.
- Chiang, E. and Goldreich, P. (1997). Spectral energy distributions of t tauri stars with passive circumstellar disks. *The Astrophysical Journal*, 490(1):368.
- Chiang, E., Joungh, M., Creech-Eakman, M., Qi, C., Kessler, J., Blake, G., and Van Dishoeck, E. (2001). Spectral energy distributions of passive t tauri and herbig ae disks: grain mineralogy, parameter dependences, and comparison with infrared space observatory lws observations. *The Astrophysical Journal*, 547(2):1077.
- Collings, M. P., Anderson, M. A., Chen, R., Dever, J. W., Viti, S., Williams, D. A., and McCoustra, M. R. S. (2004). A laboratory survey of the thermal desorption of astrophysically relevant molecules. *Monthly Notices of the Royal Astronomical Society*, 354(4):1133–1140.
- Dubrulle, B., Morfill, G., and Sterzik, M. (1995). The dust subdisk in the protoplanetary nebula. *Icarus*, 114(2):237–246.
- Exoplanet-Database (1995-2020). *Paris Observatory*. Last Accessed on 14-07-2020.
- Garrod, R. T. and Herbst, E. (2006). Formation of methyl formate and other organic species in the warm-up phase of hot molecular cores. *Astronomy & Astrophysics*, 457(3):927–936.
- Heays, A., Bosman, AD, v., and Van Dishoeck, E. (2017). Photodissociation and photoionisation of atoms and molecules of astrophysical interest. *Astronomy & Astrophysics*, 602:A105.
- Herrero, V. J., Gálvez, Ó., Maté, B., and Escribano, R. (2010). Interaction of CH<sub>4</sub> and h<sub>2</sub>o in ice mixtures. *Physical Chemistry Chemical Physics*, 12(13):3164.
- Hudgins, D., Sandford, S., Allamandola, L., and Tielens, A. (1993). Mid- and far-infrared spectroscopy of ices-optical constants and integrated absorbances. *The Astrophysical Journal Supplement Series*, 86:713–870.
- Kamp, I., Thi, W.-F., Woitke, P., Rab, C., Bouma, S., and Menard, F. (2017). Consistent dust and gas models for protoplanetary disks-ii. chemical networks and rates. *Astronomy & Astrophysics*, 607:A41.
- Kruger, E. (2002). *The physics of interstellar dust*. CRC Press.
- Maaskant, K., de Vries, B. L., Min, M., Waters, L., Dominik, C., Molster, E., and Tielens, A. (2015). Location and sizes of forsterite grains in protoplanetary disks-interpretation from the herschel digit programme. *Astronomy & Astrophysics*, 574:A140.
- Mann, R. K. and Williams, J. P. (2010). A submillimeter array survey of protoplanetary disks in the orion nebula cluster. *The Astrophysical Journal*, 725(1):430.

- Martonchik, J. V., Orton, G. S., and Appleby, J. F. (1984). Optical properties of nh 3 ice from the far infrared to the near ultraviolet. *Applied optics*, 23(4):541–547.
- Mayor, M. and Queloz, D. (1995). A jupiter-mass companion to a solar-type star. *Nature*, 378(6555):355–359.
- Natta, A., Testi, L., Calvet, N., Henning, T., Waters, R., and Wilner, D. (2006). Dust in proto-planetary disks: properties and evolution. *arXiv preprint astro-ph/0602041*.
- Schmitt, B., Bollard, P., Albert, D., Garenne, A., Gorbacheva, M., Bonal, L., Volcke, P., and and, t. S. P. C. (2017). Sshade: "solid spectroscopy hosting architecture of databases and expertise".
- Theys, N., Campion, R., Clarisse, L., Brenot, H., van Gent, J., Dils, B., Corradini, S., Merucci, L., Coheur, P.-F., Roozendael, M. V., Hurtmans, D., Clerbaux, C., Tait, S., and Ferrucci, F. (2013). Volcanic SO<sub>2</sub> fluxes derived from satellite data: a survey using OMI, GOME-2, IASI and MODIS. *Atmospheric Chemistry and Physics*, 13(12):5945–5968.
- Tielens, A. G. (2005). *The physics and chemistry of the interstellar medium*. Cambridge University Press.
- van Dishoeck, E. F., Jonkheid, B., and van Hemert, M. C. (2006). Photoprocesses in protoplanetary disks. *Faraday Discussions*, 133:231.
- Walsh, C., Millar, T. J., Nomura, H., Herbst, E., Weaver, S. W., Aikawa, Y., Laas, J. C., and Vasyunin, A. I. (2014). Complex organic molecules in protoplanetary disks. *Astronomy & Astrophysics*, 563:A33.
- Warren, S. G. (1984). Optical constants of ice from the ultraviolet to the microwave. *Applied optics*, 23(8):1206–1225.
- Williams, J. P. and Cieza, L. A. (2011). Protoplanetary disks and their evolution. *Annual Review of Astronomy and Astrophysics*, 49:67–117.
- Woitke, P., Min, M., Pinte, C., Thi, W.-F., Kamp, I., Rab, C., Anthonioz, F., Antonellini, S., Baldwin-Saavedra, C., Carmona, A., et al. (2016). Consistent dust and gas models for protoplanetary disks-i. disk shape, dust settling, opacities, and pabs. *Astronomy & Astrophysics*, 586:A103.

